Title
THE HIGH TEMPERATURE FAILURE OF CERAMICS

Author
Evans, A.G.

Publication Date
1982

LBL-13839
Preprint

Lawrence Berkeley Laboratory
UNIVERSITY OF CALIFORNIA

Materials & Molecular Research Division

To be published as a chapter in CREEP AND FRACTURE OF ENGINEERING MATERIALS, Pineridge Press, Ltd., Swansea, UK

THE HIGH TEMPERATURE FAILURE OF CERAMICS

A.G. Evans

January 1982

Prepared for the U.S. Department of Energy under Contract DE-AC03-76SF00098

DISCLAIMER

THE HIGH TEMPERATURE FAILURE OF CERAMICS*

A.G. Evans

Materials and Molecular Research Division, Lawrence Berkeley Laboratory and Department of Materials Science and Mineral Engineering, University of California, Berkeley, California 94720, U.S.A.

ABSTRACT

This review describes the various cavitation mechanisms that operate in single phase and two phase ceramic polycrystals at elevated temperatures. Analysis of these mechanisms has been used to develop failure models and thereby, to provide failure time expressions suitable for the interpretation of rupture experiments and for the eventual prediction of failure. The failure processes have been distinguished on the basis of crack nucleation control and crack propagation control. The former yields either Monkman-Grant failure expressions or probabilistic Orr-Sherby-Dorn failure relations, depending upon the cavitation homogeneity and the level of the applied loading. The available creep rupture data has been analyzed from an informed perspective provided by the failure models.

1. INTRODUCTION

The mechanical failure of ceramics at elevated temperatures is accompanied by permanent deformation and exhibits a strong dependence on temperature and strain-rate (Fig. 1). The failure usually evolves by the nucleation, growth and coalescence of cavities at preferred microstructural sites (Fig. 1). The deduction of comprehensive engineering expressions for high temperature failure requires that the cavity evolution process be understood at the fundamental

---

*This work was supported by the Director, Office of Energy Research, Office of Basic Energy Sciences, Materials Science Division of the U.S. Department of Energy under Contract No. DE-AC03-76SF00098.

level. This review describes the essential details that underlie the engineering analysis of failure.

High temperature failure typically involves several sequential processes: cavity nucleation, cavity propagation, crack nucleation and crack propagation (Fig. 2). Each process must be comprehensively characterized in order to establish a generalized description of failure. Consequently, the first part of this review is concerned with a characterization of crack nucleation (by a cavity nucleation, propagation and coalescence sequence); while the second part is devoted primarily to crack propagation processes. The implicatons for microstructural design are presented in the final section.

The analysis of high temperature failure in ceramics must be cognizant of the variety of microstructures that may exist and their influence on the specific failure evolution mechanisms. The two most important classes of ceramic microstructure are emphasized in this paper: predominantly single phase polycrystals (albeit, in some instances, with small isolated second phase particles at two grain interfaces) (Fig. 2a), and two phase systems with a continuous second phase (Fig. 3). The former microstructure typifies materials fabricated by solid state sintering, chemical vapor deposition etc., while the latter microstructure is characteristic of liquid phase sintered ceramics. An important theme of this paper will be the vital influence of second phases on the failure process at high temperatures.

The creep deformation of most commercial ceramics occurs by diffusion, viscous flow or solution/reprecipitation and consequently, exhibits a stress exponent, n, in the range $1 \lesssim n < 2$ (dislocation creep is rarely observed) [1,2]. The analysis of creep rupture in ceramics [3] is thus frequently based on a deformation linearity premise (which appears to provide an adequate first order characterization of the observed rupture behavior). The analytic simplicity afforded by linearity will be adopted in the present review.

The paucity of comprehensive creep rupture data for ceramics, especially data accompanied by microstructural observations of failure evolution, limits the present ability to provide a well-balanced view of the creep rupture process. The intent of this review is thus to provide a description of the underlying failure phenomena that establishes the eventual basis for interpreting failure data and predicting failure.

2. CRACK NUCLEATION CONCEPTS

Crack nucleation during high temperature creep generally occurs by the nucleation, growth and coalescence of cavities [3-8]. Each of these processes requires separate consideration,

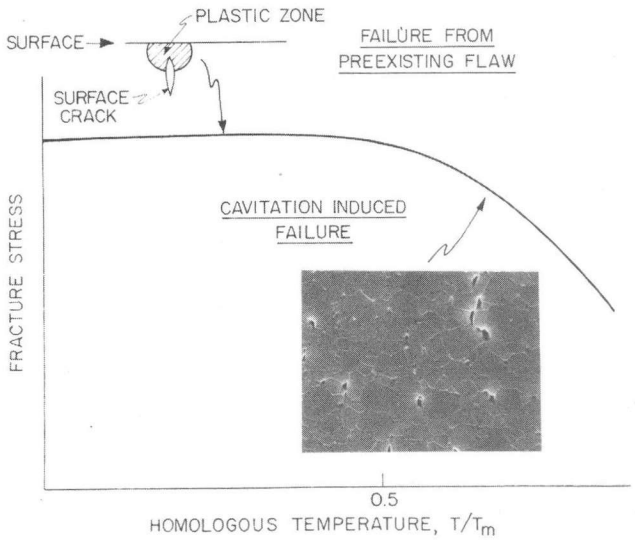

XBB813-2479

Fig. 1. A schematic of the temperature dependence of the strength of a typical ceramic polycrystal.

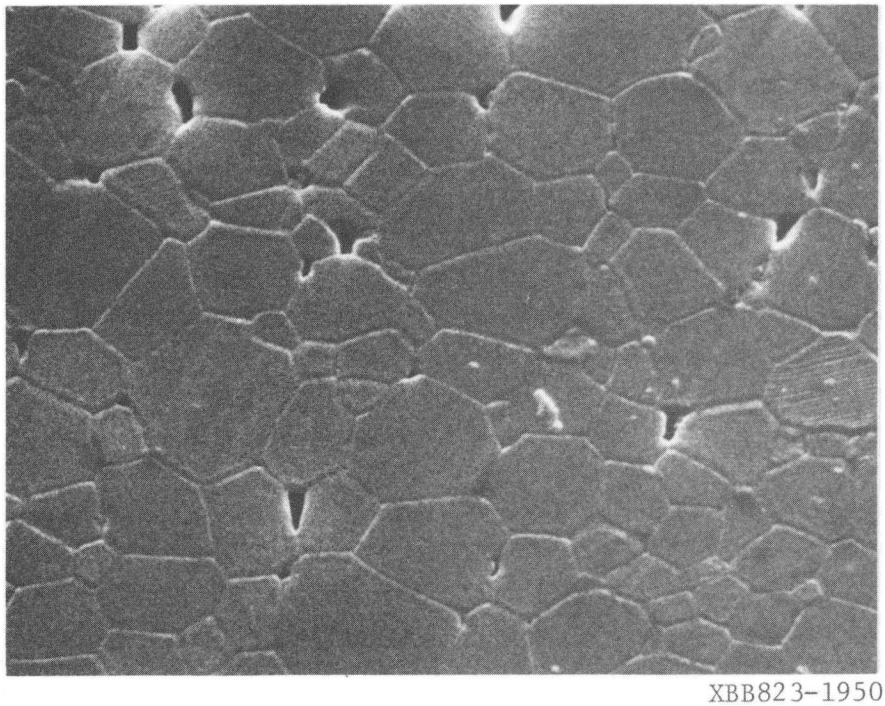

XBB823-1950

Fig. 2a. Scanning electron micrograph illustrating the processes of crack nucleation, involving nucleation and propagation.

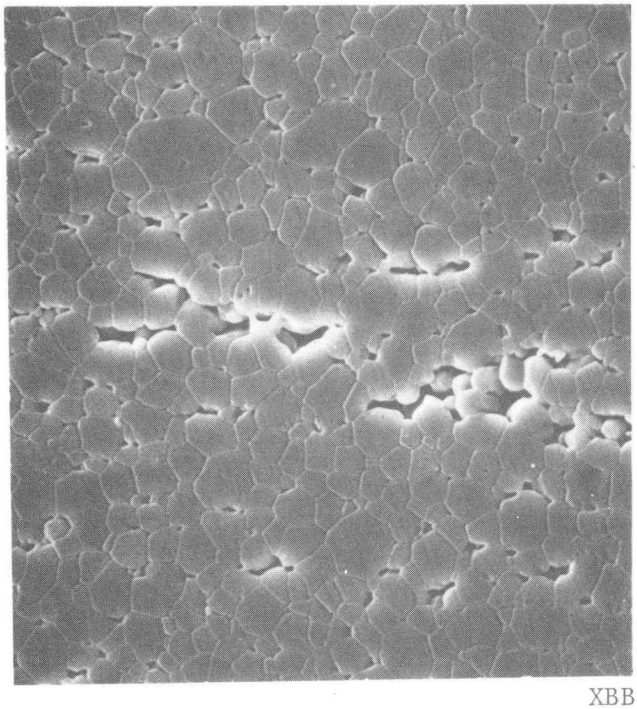

XBB 814-3790

Fig. 2b. Scanning electron micrograph illustrating the process of crack nucleation, involving cavity coalescence.

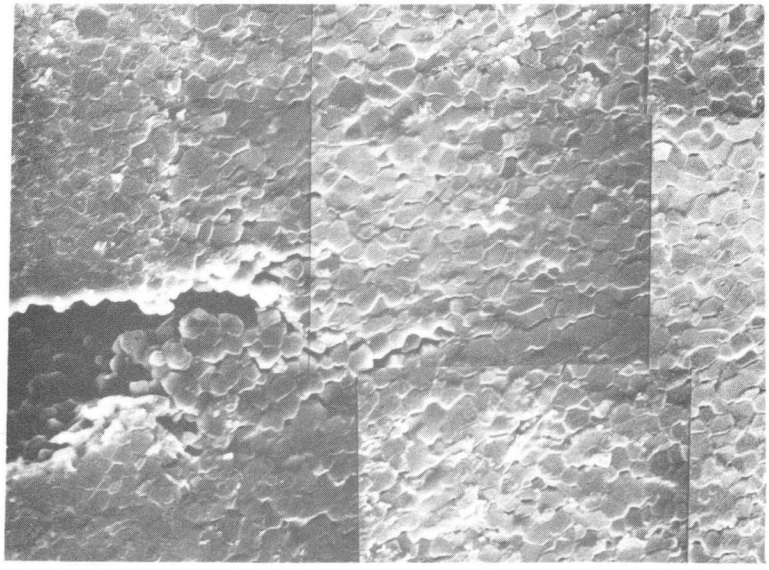

XBB 817-6185

Fig. 2c. Scanning electron micrograph illustrating the process of crack propagation.

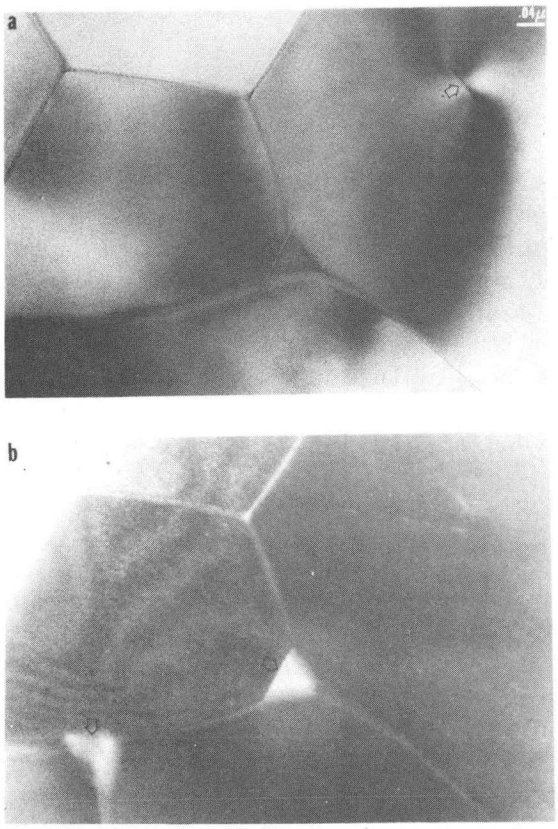

Fig. 3. Transmission electron micrographs of a Si_3N_4 material with a continuous second phase, transmission electronmicrograph. XBB810-11470

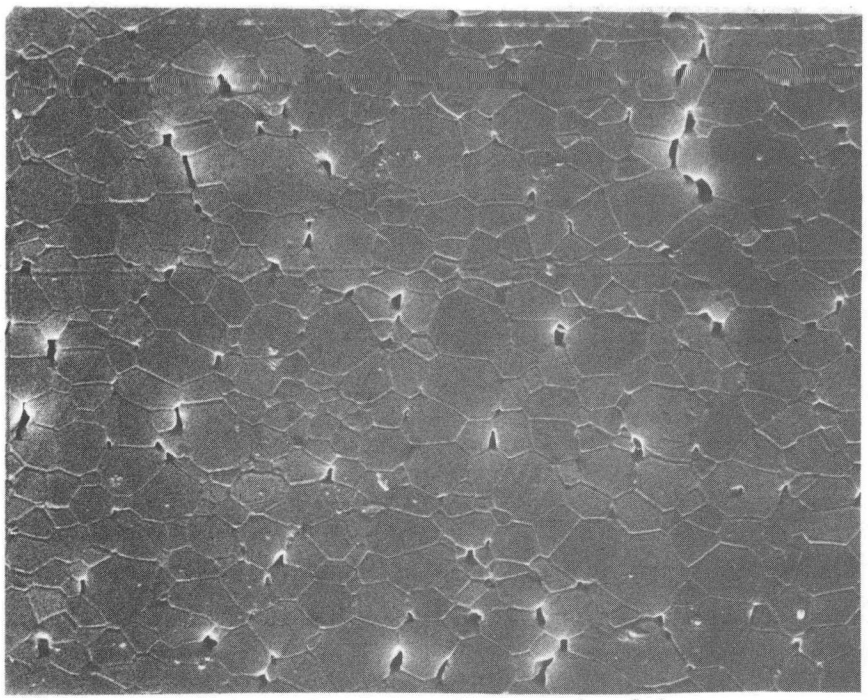

Fig. 4. A scanning electron micrograph of heterogeneous cavitation in polycrystalline Al_2O_3. XBB804-4499

as detailed in the following sections. A common theme will be the role of microstructural heterogeneity on the observed cavitation (Fig. 4) and on the resultant crack nucleation characteristics. The inhomogeneity undoubtedly exhibits a direct link with the probabilistic aspects of failure and thus constitutes an essential ingredient in the formulation of engineering failure relations. Additionally, inhomogeneous cavitation can result in appreciable changes in the local stress (constraint) that both modifies the cavity growth rates and exerts a strong influence on the cavity coalescence process. Constraint in the presence of inhomogeneous cavitation is thus afforded separate attention.

2.1 The development of constraint

When cavities form within an isolated microstructural region, the local volume change is constrained by the surrounding material and induces modified local stresses [5,9,10]. The resultant stresses are dictated by the relative rates of cavity volume change and creep relaxation. The stress distributions in a polycrystalline aggregate are complex, and their rigorous determination requires extensive numerical computation. However, an approximate analytic solution pertinent to linear materials permits both the identification of the important creep rupture parameters and elucidates the essential trends. The analysis [5] is based upon a continuum solution for the transformation of a particle in a viscoelastic solid, and requires cavitation to occur within a zone of diameter d (Fig. 5), such that matter deposition on the intervening boundaries proceeds at a rate which differs from the average mass transport rate in the surrounding material (Fig. 5a). The enhanced matter deposition, δ, that occurs in time, Δt, induces rigid body displacements of the juxtaposed grains which, if unconstrained, would produce a shape change in the zone comprising these grains (Fig. 5b). The unconstrained shape change is analgous to a transformation strain, e_{ij}^T, [11] as depicted in Fig. 5c. Maintaining conformance of the 'transformation' zone with the surrounding, 'matrix' grains induces a constraint p_{ij}^I on the transformation zone and corresponding stresses in the matrix (Fig. 5d).

The constraint p_{ij}^I is dictated by the unconstrained transformation strain rate, $\dot{e}_{ij}^T$, and by the effective viscosities η of the transformation zone and matrix. The unconstrained strain-rate is the net cavity volume change that occurs within a specified time increment, Δt. Hence, since cavitation proceeds in response to stresses normal to the cavitating boundary, the appropriate $\dot{e}_{ij}^T$ derives from the cavity volume change in the presence of the resultant normal stress acting during the interval, Δt. The transformation strain is partially accommodated by viscous relaxation of

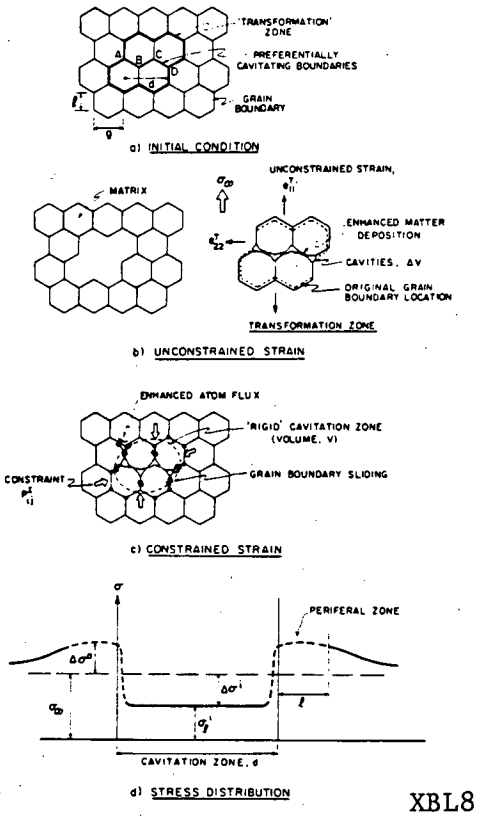

XBL813-5321

Fig. 5. A schematic of the constraint developed by inhomogeneous cavitation, (a) the initial condition, (b) the unconstrained strain, (c) the constrained strain, (d) the stress distribution.

the shear stresses during Δt (within both the transformation zone and the matrix). The resultant constrained stress determines p_{ij}^{I}.

The viscous deformation involves grain boundary sliding and diffusive flow [12]. The viscosity assigned to this mode of deformation depends upon the number of grains participating in the relaxation process (especially those grains at the periphery of the cavitation zone, Fig. 5c, where the shear stresses are most intense). The viscosity approaches the continuum value for the polycrystalline aggregate, $\eta_{cont.}$, [12] when a sufficiently large number of grains are involved;

$$\eta_{cont.} \equiv \sigma_{\infty}/\dot{\varepsilon}_{\infty} = 3\sqrt{3}\ell^{3}kT/14\Omega(\sqrt{3}\ell D_{\ell} + \pi D_{b}\delta_{b}) \quad , \qquad (1)$$

where $D_{b}\delta_{b}$ is the grain boundary diffusion parameter, D_{ℓ} is the lattice diffusivity, Ω is the atomic volume, ℓ is the grain facet length, σ_{∞} is the applied stress and $\dot{\varepsilon}_{\infty}$ is the steady-state creep rate. It is assumed, for present purposes, that cavitation zones consisting of at least three grain facets (Fig. 5) embrace an adequately large number of peripheral grains ($\sim$30 peripheral grains for the three-dimensional zone subject to analysis).

The transformation strain-rate $\dot{e}_{ij}^{T}$ is determined by the distribution of matter deposition within the cavitation zone. It is a function of both the total cavitation volume, ΔV, the distribution of grain boundary orientations within the cavitation zone, and the zone shape. The general solution, which contains both deviatoric and dilational components, is unwiedly. Hence, specific results are presented for the two limits of most significance.

When the cavitation zone diameter is relatively small (such as the three cavitating facets depicted in Fig. 5), the constraint is essentially the same as that expected for a purely dilational transformation. The zone can therefore be considered subject to a dilation dictated exclusively by the cavitation volume, ΔV. Consequently, by equating the cavitation zone volume to that of a spheroidal region of equivalent size (Fig. 5c);

$$V \approx (\pi/3)d^{2}\ell \quad , \qquad (2)$$

the transformation strain rate becomes;

$$\dot{e}^{T} \approx 3\dot{\Delta V}/\pi d^{2}\ell \quad . \qquad (3)$$

This dilational strain results in a shape independent, upper bound constraint, given by;

$$p^I = -4\dot{e}^T\eta/3 \equiv -4\dot{\Delta V}\sigma_\infty/\pi d^2 \ell \dot{\varepsilon}_\infty \quad , \tag{4}$$

and the local tension $\sigma_\ell{}^i$ normal to the cavitating boundaries becomes;

$$\sigma_\ell^i = \alpha\sigma_\infty - p^I/3 \quad , \tag{5}$$

where α is determined by the inclination of the boundary to the applied stress axis. Conservation of matter within the zone requires that;

$$\dot{\Delta V} \approx (\pi/3)d^2\dot{\delta} \quad , \tag{6}$$

where $\dot{\delta}$ is determined by the cavity growth mechanism. Hence,

$$p^I = -4\dot{\delta}\sigma_\infty/3\ell\dot{\varepsilon}_\infty \quad . \tag{7}$$

Specifically, for viscosities characterized by equation (1), the constraint becomes;

$$p^I \approx -\left(\frac{6\sqrt{3}}{7}\right)\frac{\ell^2\dot{\delta}kT}{\Omega(\sqrt{3}\ell D_\ell + \pi D_b\delta_b)} \quad , \tag{8}$$

and the local tensile stress normal to the cavitating boundaries depicted in Fig. 5 is given for fine grained materials ($\ell D_\ell << D_b\delta_b$) by

$$\sigma_\ell^i \approx \left(\frac{3}{4}\right)\sigma_\infty - \left(\frac{2\sqrt{3}}{7\pi}\right)\frac{\ell^2\dot{\delta}kT}{\Omega D_b\delta_b} \quad . \tag{9}$$

Other grain orientations yield slightly different results. The constraint reduces to a lower level than given by equation (9) when the zone approaches a free surface or, when an array of such zones, separated by <d, interact.

When the cavitation zone enlarges, such that $d > 6\ell$, an appreciable deviatoric stress develops, and the problem resembles that of a crack, diameter d, subject to opening displacements that accommodate the enhanced matter deposition along the intervening grain facets. The crack solution, pertinent to the large zone size limit, provides a constraint along the applied stress axis [5];

$$p_{11}^{I} \equiv -\frac{3\pi\eta\dot{\delta}}{2d} = -\frac{9\sqrt{3}}{28}\frac{\dot{\delta}\ell^2 kT}{\Omega D_b \delta_b}\left(\frac{\ell}{d}\right) \quad . \tag{10}$$

The tangential stresses outside the original cavitation zone are enhanced by the constraint on the cavity volume change. The stresses on those boundaries contiguous with the cavitating boundaries are of principal interest, because these stresses dictate the zone expansion and cavity coalescence processes that result in eventual crack nucleation. The stresses relate to the continuum stresses, as redistributed by local grain boundary sliding and diffusion. It may be assumed that the stress redistribution is confined primarily to those boundaries immediately adjacent to the cavitation zone; such that the average stress on the peripheral boundaries is similar to the average continuum stress. Cavity growth in the peripheral zone can then proceed at a rate dictated by this average stress. The upper bound continuum stress for the small cavitation zone, subject to dilation, is;

$$\sigma_\ell^0 \approx (p^I/3)(\ell/x)^3 + (3/4)\sigma_\infty \quad , \tag{11a}$$

where x is the distance from the center of the cavitation zone. The average stress on the first peripheral zone is thus;

$$\langle\sigma\rangle_\ell^0 \approx p^I/8 + (3/4)\sigma_\infty \quad . \tag{11b}$$

The equivalent solutions at the large zone limit are;

$$\sigma_\ell^0 = \sigma_\infty + p_{11}^I \left\{1 - x\left[x^2-(d/2)^2\right]^{-1/2}\right\} \quad , \tag{12a}$$

$$\langle\sigma\rangle_\ell^0 = \sigma_\infty + p_{11}^I - \frac{p_{11}^I}{4\ell(\ell+d)}\left[2(d+2\ell)\sqrt{(\ell^2+\ell d)}\right.$$

$$\left. + d^2 \ln\left(\frac{d+2\ell+2\sqrt{(\ell^2+\ell d)}}{d}\right)\right] \quad . \tag{12b}$$

2.2 Cavity nucleation

In the absence of pre-existent porosity, the first step in the high temperature failure process consists of the nucleation of either cavities on grain boundaries or holes within viscous phases. The nucleation process is generally considered to involve a critical nucleus formed by the local accumulation of vacancies in a region subject to tensile stress. Cavity nucleation by vacancy coalescence can be treated using standard nucleation concepts [13] to demonstrate

that a critical stress σ_c is needed to induce stable cavities and that this critical stress depends on the location of the nucleation site. The critical stress is determined by firstly identifying the condition, during cavity formation, that dictates the maximum change in thermodynamic potential. The potential contains terms due to the work done against the local stress during a cavity volume increment, ΔV, and terms associated with the change in surface and grain boundary areas, ΔA_s and ΔA_b, respectively, such that

$$\Delta\phi = -\sigma\Delta V + \gamma_s \Delta A_s - \gamma_b \Delta A_b \quad . \tag{13}$$

A critical nucleus exists when $\Delta\phi = 0$, as given by;

$$r^* = 2\gamma_s/\sigma^*$$

$$\sigma^* = \gamma_s (dA_s/dV)^* - \gamma_b (dA_o/dV)^* \quad , \tag{14}$$

where the asterisk indicates that parameters are evaluated at critical size r*. The critical nucleus concept can be used to deduce the critical stress by obtaining the cavity nucleation rate from the product of the number of nuclei at the critical size and the probability that a vacancy will be added to the critical nucleus [13]. The general result for a grain boundary located cavity is given by [13];

$$(\sigma^*)^2 \approx \frac{4\gamma_s^3 F_V(\psi)}{kT} \ell n \left[4\pi z \gamma_s D_b \delta_b \eta_o / \sigma^* \Omega^{4/3}\right] \quad , \tag{15}$$

where z is Zeldovich's factor ($\sim 10^{-2}$), ψ is the dihedral angle, $F_V(\psi)$ is a function that depends on the void location and η_o is the number of available nucleation sites per unit area of grain boundary. For a nucleus located on a two grain interface (Fig. 6a) [13];

$$F_V(\psi) = (2\pi/3)\left[2-3\cos(\psi/2) + \cos^3(\psi/2)\right] \quad .$$

A typical trend in the critical stress for nucleation on two grain interfaces in Al_2O_3 (plotted in Fig. 7) indicates that, for typical dihedral angles ($\psi \gtrsim \pi/2$), the stress is many times larger than the applied stress levels ($\gtrsim$ 50 MPa) known to initiate cavities at grain boundaries during creep tests. The resolution of this dilemma probably resides in a combination of two effects. A substantial reduction in the critical nucleation stress can be obtained when nucleation occurs either at three or four grain interfaces, at inclusions or within second phases. Also, stress concentrations can develop in creeping solids in the presence either of grain boundary sliding transients or of microstructural inhomogeneity.

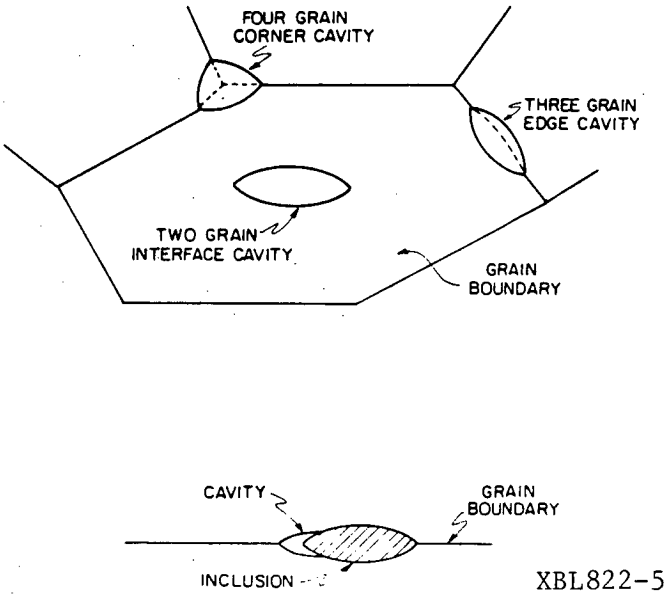

Fig. 6. Schematics of potential cavity nucleation sites in polycrystals, (a) cavities on grain interfaces, (b) a cavity at a grain boundary inclusion.

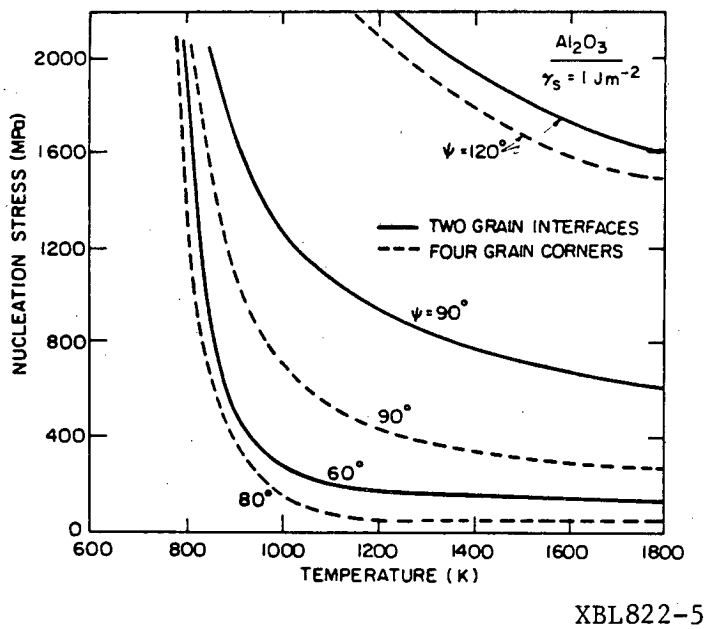

Fig. 7. The critical cavity nucleation stress in Al_2O_3 for cavities on two grain interfaces and at four grain corners, plotted for several dihedral angles.

A reduced critical nucleation stress is generally the direct consequence of a cavity morphology change that increases the relative change in volume to surface area during cavity enlargement (Eq. 2): as achieved by inducing maximum deviations from sphericity. Thus cavitation at three or four grain corners (Fig. 6 a) often occurs more readily than on two grain interfaces. Additionally, the critical stress exhibits a strong dependence on dihedral angle. For example, cavities on four grain corners nucleate spontaneously (at zero stress) when $\psi = 70°$ and quite readily when $\psi < 90°$ (Fig. 7), as expressed by the critical stress parameter [13];

$$F_V(\psi) = 8\left\{\pi/3-\cos^{-1}\left[\left[\sqrt{2}-\cos(\psi/2)\ (3-A^2)^{1/2}\right]/A\ \sin(\psi/2)\right]\right\}$$
$$+ A\ \cos(\psi/2)\left[(4\ \sin^2(\psi/2) - A^2)^{1/2} - A^2/\sqrt{2}\right]$$
$$- 4\ \cos(\psi/2)\left[3-\cos^2(\psi/2)\right]\ \sin^{-1}\left[A/2\ \sin(\psi/2)\right] , \qquad (16)$$

where,

$$A = (2/3)\ \left[\sqrt{2}(4\ \sin^2\psi/2-1)^{1/2} - \cos(\psi/2)\right] .$$

Equivalently, inclusions can be a major source of premature cavity nucleation, whenever the inclusion has an associated dihedral angle appreciably smaller than the equivalent matrix angle (Fig. 6b). A typical nucleation stress in the presence of a grain boundary inclusion is given by the nucleation parameter [13];

$$F_V(\psi) \approx (4\pi/3)\ \{2-3\left[\cos(\psi/2+\beta-\mu)/2\right] + \cos^3(\psi/2+\beta-\mu)/2\} ,$$

where

$$\beta = \cos^{-1}\left[(\gamma_{ib}-\gamma_i)/\gamma_s\right] \quad \text{and} \quad \mu = \cos^{-1}(\gamma_b/2\gamma_{ib}) , \qquad (17)$$

where γ_i is the energy of the inclusion free surface and γ_{ib} is the energy of the inclusion/matrix interface.

A continuous amorphous phase often provides an alternate source of premature cavitation in certain ceramics, by virtue of the relatively smaller surface energy of the amorphous phase ($\sim$0.2 Jm^{-2} for many amorphous phases compared with $\sim$1 Jm^{-2} for crystalline phases). Nucleation occurs by the formation of holes with the amorphous phase. Such materials are a typical consequence of liquid phase sintering and the existence of amorphous enclaves at three grain channels is common [14,15] (Fig. 8).(i) The amorphous pockets can be

---

(i) The enclaves are a consequence of anisotropy in the interface energy, resulting in facetted interfaces.

large enough to include a spherical hole of critical size (Fig. 8) and the critical stress becomes the stress needed to nucleate a hole in that volume of liquid encompassed by the amorphous pockets, as given by [15,16];

$$\sigma_c^2 \approx \left(\frac{16\pi\gamma^3}{3kT}\right) \ell n \left[\frac{3\eta\Omega^{5/3}\sigma_c^2}{8\gamma^2 kTV_f}\right] , \qquad (18)$$

where η is the viscosity of the amorphous phase and V is the volume concentration of amorphous pockets. In the absence of pockets at three grain channels, the holes must nucleate along two grain interfaces, which are frequently too narrow to support a spherical hole of critical size. The cavities then exhibit the morphology of oblate holes (Fig. 9), characterized by a volume/area ratio smaller than that associated with the spherical hole. The critical stress thus exceeds that required for spherical hole nucleation, as given by [15];

$$\frac{\sigma_c\delta}{\gamma} = \left(\frac{\pi-8}{4\pi^2}\right) + \frac{2kT}{\pi^3\gamma\delta^2} \ell n \left[\frac{3\eta\Omega^{5/3}\sigma_c}{2\gamma\delta kTV_f^*}\right]$$

$$+ \left\{\left[\left(\frac{\pi-8}{4\pi^2}\right) + \frac{2kT}{\pi^3\gamma\delta^2} \ell n \left(\frac{3\eta\Omega^{5/3}\sigma_c}{2\gamma\delta kTV_f^*}\right)\right]^2 - \left(\frac{3\pi^2-32}{48\pi^2}\right)\right\}^{1/2} . \qquad (19)$$

where V_f^* is the volume concentration of amorphous material within two grain channels. Some typical hole nucleation trends for a liquid phase sintered Si_3N_4 are shown in Fig. (10).

The reduced critical cavity nucleation stresses associated with grain corners, inclusions or amorphous phases are generally still in excess of the applied stress levels at which cavities are observed to form. It is thus concluded that stress concentration effects are frequently involved in cavity nucleation. The dominant source of stress concentration during creep is the sliding of grain boundaries [17,18]. The relaxation of shear stress along sliding boundaries transmits additional stress to the stationary boundaries. For example, in a simple hexagonal grain array (Fig. 11), when the sliding boundaries are fully relaxed, the stationary boundaries support an average stress that exceeds the applied stress, σ_∞, by ~2 [19], while the tension in the sliding boundaries is reduced to zero. However, transient stresses of larger amplitude may be of greater significance. Large stresses develop following relatively abrupt grain boundary sliding transients, with a peak tensile stress [18];

$$\hat{\sigma} \approx 0.4\sigma_\infty \sqrt{\ell} \left(GD_b\delta_b\Omega t_\ell/(1-\nu)kT\right)^{-1/6} , \qquad (20)$$

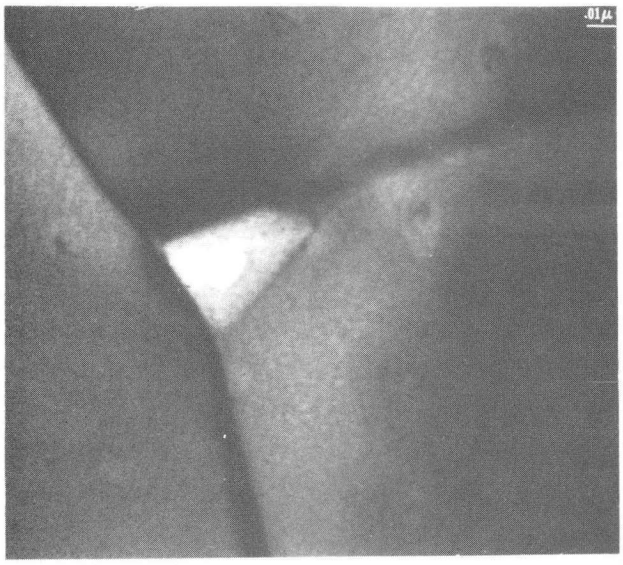

Fig. 8. A transmission electron micrograph of a hole formed within an amorphous pocket in Si_3N_4. (XBB810-11469)

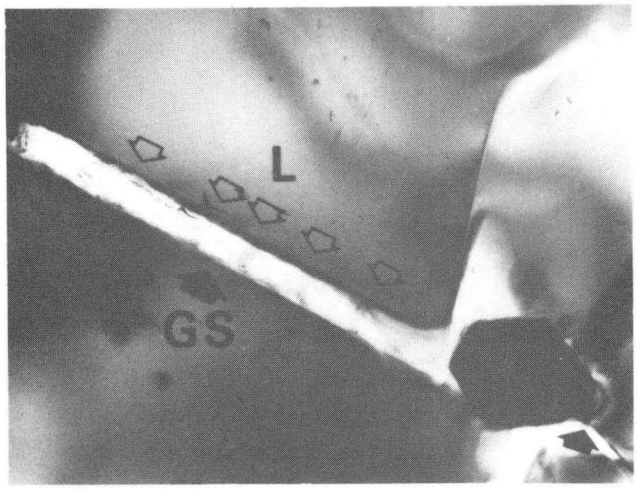

Fig. 9. A transmission electron micrograph of oblate holes within an amorphous phase along a two grain channel in Si_3N_4 (courtesy of D.R. Clarke). (XBB823-1951)

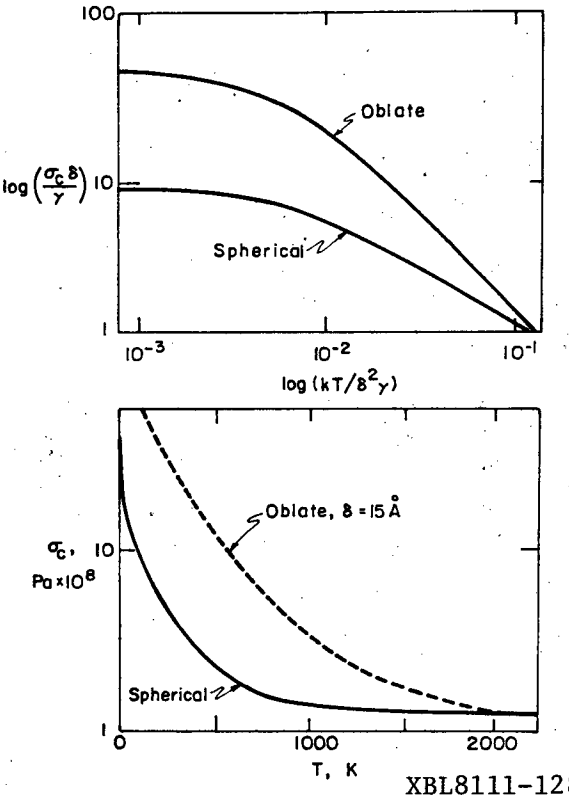

XBL8111-12865

Fig. 10. The critical hole nucleation stresses, (a) in normalized coordinates, (b) specific results for Si_3N_4.

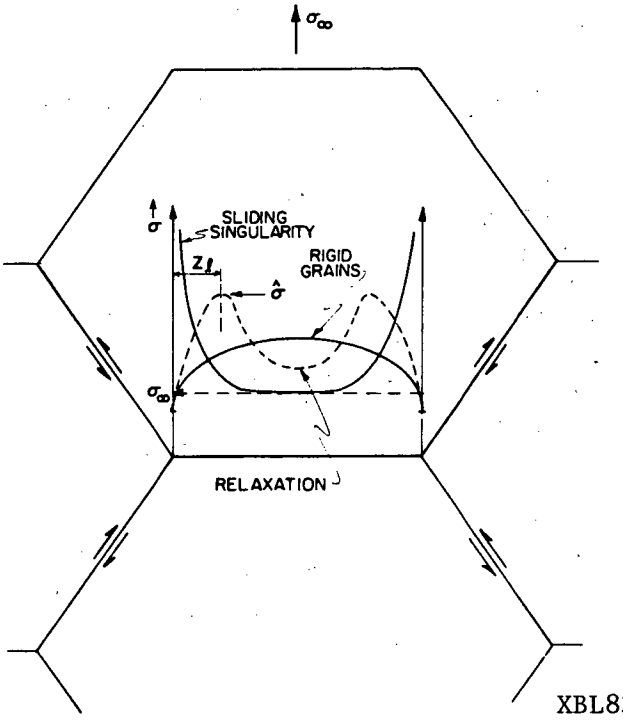

XBL822-5268

Fig. 11. A schematic illustrating the stress redistribution that occurs due to grain boundary sliding and diffusive flow.

where ℓ is the length of the freely sliding boundary (i.e., either the total length of the sliding boundary or the distance between impeding ledges, or inclusions), G is the shear modulus, and t_ℓ is the duration of the sliding transient. The maximum stress occurs at a distance [18], (Fig. 11)

$$z_\ell \approx 1.3(GD_b\delta_b\Omega t_\ell/(1-\nu)kT)^{1/3} , \qquad (21)$$

from the position (ledge or corner) that impedes the sliding. It is tempting to invoke these transient sliding induced stresses as the source of grain boundary cavities [17]. However, caution should be exercised in applying transient related nucleation concepts until adequate attention has been devoted to a comprehension of the mechanism and duration of grain boundary sliding transients and to the duration of the stress concentration, $\hat{\sigma}$ (vis-a-vis, the time needed to nucleate a stable cavity). Neither of these topics has yet been examined in convincing detail.

Although a reasonable comprehension of the important issues involved in cavity nucleation in ceramic polycrystals has recently been developed, a satisfactory quantitative interpretation does not exist (primarily by virtue of an incomplete knowledge of grain boundary sliding transients). Nevertheless, the strong effects of dihedral angle that result in relatively easy nucleation in the range $70° < \psi < 110°$ (Eq. (16)), have lead to suggestions that cavities nucleate readily in polycrystalline ceramics [4,5], on that proportion of grain boundaries that exhibit low dihedral angles. However, direct evidence for this hypothesis does not exist, and nucleation should be regarded as an unresolved issue until further study has been completed.

The nucleation requirement can, of course, be negated if the as-sintered material contains appreciable remnant porosity at grain boundaries. In this context, it is interesting to note that the final removal of porosity during sintering becomes increasingly difficult when the dihedral angle approaches 70°. The tendency for porosity retention on low dihedral angle boundaries is consistent with the relative ease of cavity nucleation (and growth) along these same boundaries. The spectrum of dihedral angles in polycrystalline ceramics (and its dependence on the range of grain boundary and surface energies) thus emerges as a central feature of high temperature failure in ceramics.

2.3 Cavity growth mechanisms

The cavity growth rates in ceramics depend upon the spatial density and location of cavity nucleation sites and upon the mechanism of cavity growth. The cavity growth mechanisms are sufficiently distinct for materials that

include a continuous, amorphous phase that these materials are examined separately. All other materials are regarded as 'single' phase with regard to their cavity growth behavior (inclusions, or precipitates, often dictate cavity nucleation propensities, but are presumed to exert a minimal influence on cavity propagation).

Before embarking upon specific analyses of cavity growth, some general considerations are presented. Problems of cavity growth are invariably analyzed by performing a series of inter-related calculations. For diffusive cavitation, the diffusion equations pertinent to the atom flux over the cavity surface (dictated by the curvature gradient) and along the grain boundary (determined by the normal stress gradient) are firstly solved, yielding the relations [5,20,21];

$$\dot{\Delta V} = \dot{a} F_1 \left[D_s \delta_s \Omega \gamma_s / kT, \psi, a, \ell \right] \quad , \tag{22a}$$

$$\dot{\delta} = \left[\sigma_\ell^i - \sigma_o h(f) \right] F_2 \left[\Omega D_b \delta_b / kT, a, \ell \right] \quad , \tag{22b}$$

where $D_s\delta_s$ is the surface diffusivity, σ_o is the sintering stress, h is a function of the relative cavity size and F_n are functions that depend upon the cavity morphology and spacing. A similar pair of equations pertain to hole growth by viscous flow (with the diffusivity terms replaced by a viscosity). Conservation of matter is then invoked, by allowing the atom flux leaving the cavity tip to equal the flux entering the grain boundary, to obtain [5,21],

$$\dot{\Delta V} = \dot{\delta} F_3(a,\ell) \quad . \tag{22c}$$

Combining Eqs. (22) permits the cavity velocity to be expressed as;

$$\dot{a} = (F_3 F_2 / F_1) (\sigma_\ell^i - \sigma_o h) \quad . \tag{23}$$

Finally, the local stress is obtained (Eqs. 5 and 7) as;

$$\sigma_\ell^i \equiv \alpha \sigma_\infty - p^I/3 = \sigma_\infty \left[\alpha - \dot{\Delta V} / \dot{\varepsilon}_\infty F_4(d\underline{V}) \right] \quad , \tag{24}$$

where $\underline{V}$ is the volume of the cavitation zone.

Combining Eqs. (23) and (24) the cavity growth rate becomes,

$$\dot{a} \left[1 + \left(\frac{\sigma_\infty}{\dot{\varepsilon}_\infty \ell} \right) \frac{F_3 F_2}{F_4} \right] = \frac{F_2 F_3}{F_1} (\alpha \sigma_\infty - h \sigma_o) \quad . \tag{25}$$

The second term in the parentheses on the left hand side is simply the modification to the velocity that derives from the constraint (i.e., $\dot{a} \to \dot{a}^u$, the unconstrained velocity, as $F_4 \to \infty$ and $p^I \to 0$). Hence, the cavity growth rate can invariably be expressed in the form;

$$\dot{a} = \dot{a}^u[1 + (\sigma_\infty/\dot{\varepsilon}_\infty)\ (F_2F_3/F_4)]^{-1} \quad . \tag{25a}$$

Consequently, the cavity propagation time, t_p, obtained by applying the integral,

$$t_p = \int_{a_o}^{\ell} (1/\dot{a})da \quad , \tag{26}$$

where a_o is the initial cavity size, always separates into two components [5,10];

$$t_p = \int_{a_o}^{\ell} (1/\dot{a}_u)da + (1/\dot{\varepsilon}_\infty) \int_{a_o}^{\ell} (F_1/F_4)\ [\alpha-\sigma_o h/\sigma_\infty]^{-1}\ da$$

$$\equiv t_p^u + t_p^c \quad , \tag{27}$$

where t_p^u is the propagation time in the absence of constraint and t_p^c is the additional contribution to the propagation time provided by the constraint. Note that t_p^c has the form;

$$t_p^c\dot{\varepsilon}_\infty = T(\sigma_\infty,\psi,D_s\delta_s\Omega\gamma_s/kT,\ell,\sigma_o) \quad . \tag{28}$$

The product $t_p^c\dot{\varepsilon}_\infty$ emerges because relaxation of the volume strain within the cavitation zone is dictated by the creep rate (viscosity) of the surrounding material. Highly constrained cavitation thus anticipates Monkman-Grant behavior ($t_p\dot{\varepsilon}_\infty$ = constant) in a natural way, irrespective of the specific mechanisms of creep and cavitation.

Comparison of t_p^u with t_p^c frequently indicates that the latter is large and dominates the failure process. The circumstances appropriate to such a comparison are afforded explicit attention in the following section. In the present section, t_p^u and the 'fully-constrained' t_p^c are presented for each cavitation mechanism. It is noted, however, that the F_2 independence of $t_p^c\dot{\varepsilon}_\infty$ indicates that fully constrained cavity growth is dictated by cavity geometry and volume conservation requirements (invariant with the atom flow rate between cavities, which determines F_2). Several different atom transport mechanisms can thus be expected to yield similar fully-constrained cavitation times.

2.3.1 'Single' phase materials

Cavities in single phase ceramic polycrystals invariably form at grain boundaries, in accord with one of three morphological types: equilibrium, crack-like or finger-like. Equilibrium cavities prevail at low stresses and large cavity spacings, crack-like cavities develop at high stresses or small cavity spacings, while finger-like cavities become important at high cavity growth rates (especially in coarse-grained polycrystals). The specific rates of growth of cavities exhibiting these general morphological characteristics depend upon the cavity nucleation sites (at two, three or four grain interfaces). Observations performed on polycrystal ceramics suggest that cavity nucleation on three/four grain interfaces (Fig. 2a) prevails in fine-grained materials [4], whereas nucleation on two grain interfaces (Fig. 12) becomes increasingly important in more coarse-grained materials [22].

(a) Fine-grained materials

Cavity nucleation in fine grained materials presumably initiates at those grain corners with low dihedral angles (section 2.2), especially when subject to the transient sliding of juxtaposed grain boundaries. The cavities initially extend from their nucleation sites to occupy a three grain channel (Fig. 13a). This process occurs relatively quickly. The resultant equilibrium-shaped cavities then expand (Fig. 13b) and retain their equilibrium morphology, while the cavity is small. Retention of the equilibrium shape requires that the surface flux be sufficiently large (by virtue of a large surface curvature) that attempted deviations from curvature uniformity (as motivated by the atom flux into the boundary from the cavity tip) are instantly removed [20]. Continued expansion of the cavity reduces the surface curvature and eventually, attempted deviations from curvature uniformity are retained. Thereupon, a transition to a crack-like cavity morphology ensues, (Fig. 13c) and the resultant cavity extends preferentially along boundaries approximately normal to the applied tension [5,20]. The crack-like cavity continues to extend along the grain interface, to form a full-facet cavity (Fig. 13d). The full-facet cavities are generally resistant to extension along the contiguous boundaries and consequently increase their volume by a thickening process [4]. The length stability of the full-facet cavities is presumably a consequence of the grain boundary sliding that occurs in response to the atom flux along the cavitating boundary. This reduces the normal tension on the sliding boundaries (section 2.2) and thus reduces the boundary flux at the grain corner to a level that can be accommodated by a surface flux acting over the full length of the cavity.

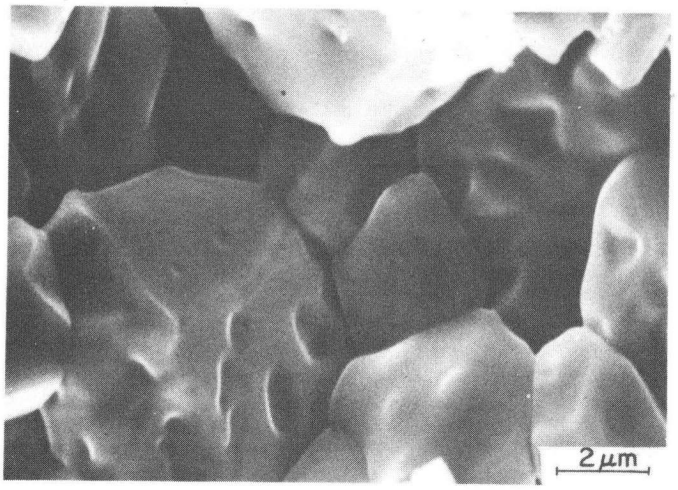

Fig. 12. Scanning electron micrograph of cavities on two grain interfaces in coarse grained (15 μm) Al_2O_3. (XBB813-2548)

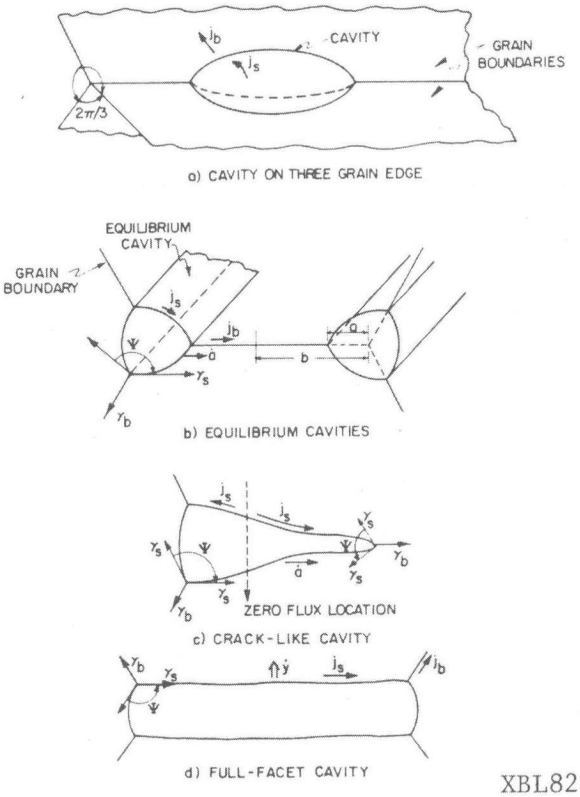

XBL822-5267

Fig. 13. A schematic illustrating the progression of a cavity from (a) nucleus on a three or four grain site to, (b) a cylindrical equilibrium cavity, (c) a crack-like cavity, (d) a full facet cavity.

The growth rate of the equilibrium cavities can be deduced by firstly evoking matter conservation which, for unit width of the cavitation zone, requires that [5,21],

$$\dot{V}_{eqm} \approx \dot{\delta}\ell \quad , \tag{29}$$

where $\dot{V}$ is the rate of volume change of an individual cavity. The volume of an equilibrium-shaped, cylindrical, triple junction cavity is (for unit width) [5]

$$V_{eqm} = 3\sqrt{3}\, a^2\, F(\psi)/4 \quad , \tag{30}$$

where a is the distance of the cavity tip from the original site of the triple junction (Fig. 13b) and

$$F(\psi) = 1 + \frac{\sqrt{3}[\psi-\pi/3 - \sin(\psi-\pi/3)]}{2\,\sin^2(\psi/2-\pi/6)} \quad . \tag{31}$$

The rate of volume change is thus;

$$\dot{V}_{eqm} = 3\sqrt{3}\, a\, \dot{a}_{eqm} (F(\psi)/2) \quad . \tag{32}$$

The cavity velocity is related to the additional matter deposition, from Eqs. (29) and (32), by;

$$\dot{\delta} = (3\sqrt{3}/4)\dot{a}_{eqm}\, f\, F(\psi) \quad , \tag{33}$$

where $f = 2a/\ell$. The matter deposition is also related to the level of the local stress over the intervening boundaries [5];

$$\dot{\delta} = \frac{12\Omega D_b \delta_b}{kT\ell^2} \frac{[\sigma_\ell^i - (1-f)\sigma_o]}{(1-f)^3} \quad , \tag{34}$$

where σ_o, the sintering stress, is given by;

$$\sigma_o = 2\gamma_s h(\psi)/\sqrt{3}\, a$$

$$h(\psi) = \sin[\psi/2 - \pi/6] \quad . \tag{35}$$

The cavity velocity is thus,

$$\dot{a}_{eqm} = \frac{16\Omega D_b \delta_b}{\sqrt{3}\, kT\ell^2} \frac{[\sigma_\ell^i - \sigma_o(1-f)]}{F(\psi)\,(1-f)^3} \quad . \tag{36}$$

The magnitude of the local stress pertinent to Eq. (36) is deduced by noting that the matter deposition given by Eq. (34) must be compatible with the development of the local stress induced by the constraint of the surrounding material. For example, using the upper bound constraint (Eq. 9) pertinent to a small cavitation zone (e.g., Fig. 5), the local stress becomes;

$$\sigma_{\ell} = [(3/4)\ (1-f^3)\sigma_{\infty} + (24\sqrt{3}/7\pi)\ (1-f)\sigma_o]$$

$$[(1-f)^3 + (24\sqrt{3}/7\pi)]^{-1} \quad . \tag{37}$$

Combining Eqs. (36) and (37) the final relation for the highly constrained cavity velocity, expressed in dimensionless form, becomes;

$$\dot{a}^c_{eqm}\left(\frac{kT\ell^3}{\Omega D_b \delta_b \gamma_s}\right) = \frac{(16/\sqrt{3})[(3/4)(\sigma_{\infty}\ell/\gamma_s)f - (4/\sqrt{3})h(\psi)(1-f)]}{F(\psi)f^2[(1-f)^3 + (24\sqrt{3}/7\pi)]} \quad , \tag{38a}$$

which reduces for $\sigma_{\infty} >> \sigma_o$ to;

$$\dot{a}^c_{eqm}\left(\frac{kT\ell^3}{\Omega D_b \delta_s}\right) \approx \left(\frac{7\pi}{6}\right)\ \frac{\sigma_{\infty}\ell}{F(\psi)} \quad . \tag{38b}$$

For unconstrained conditions, the equivalent result ($\sigma_{\infty} >> \sigma_o$) is;

$$\dot{a}^u_{eqm}\left(\frac{kT\ell^3}{\Omega D_b \delta_b}\right) \approx \left(\frac{12}{\sqrt{3}}\right)\frac{\sigma_{\infty}\ell}{F(\psi)f(1-f)^3} \quad . \tag{38c}$$

The variations of the cavity velocity with cavity length and with the dominant variables ($\sigma_{\infty}\ell/\gamma_s, \psi$) are exemplified in Figs. 14a and 15. The corresponding change in the local stress is plotted in Fig. 14(b).

The equivalent analysis of crack-like cavity growth can be conducted by noting that both the cavity profile and the atom flux at the tip of well developed crack-like cavities depend on the instantaneous cavity velocity; viz. the prior, equilibrium morphology of the cavity is of minor significance [23]. The growth process can thus be adequately treated by focusing on the tip region, and neglecting complex morphological changes that may be occurring in the vicinity of the cavity center. Commencing with the expression for the surface flux at the tip of a crack-like cavity [20]

$$\Omega J_s = 2\sin(\psi/4)\dot{a}^{2/3}_{crack}(D_s\delta_s\Omega\gamma_s/kT)^{1/3} \quad , \tag{39}$$

and noting that the surface flux is related to the volume rate of matter removal, up to the zero flux position (Fig. 13c), by;

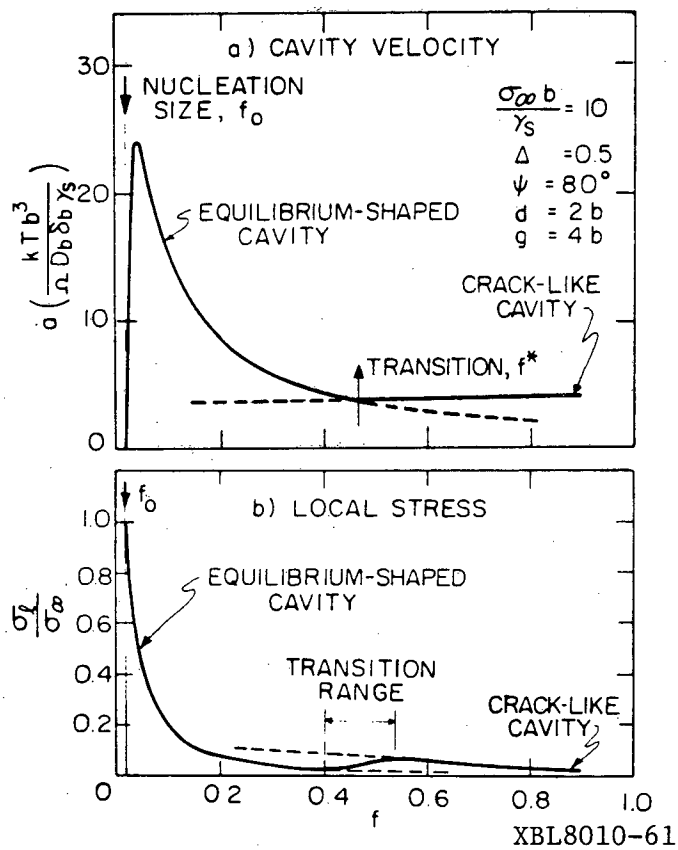

Fig. 14. (a) The variation in cavity velocity with cavity length, indicating the crack like transition, (b) the change in the local stress with cavity length.

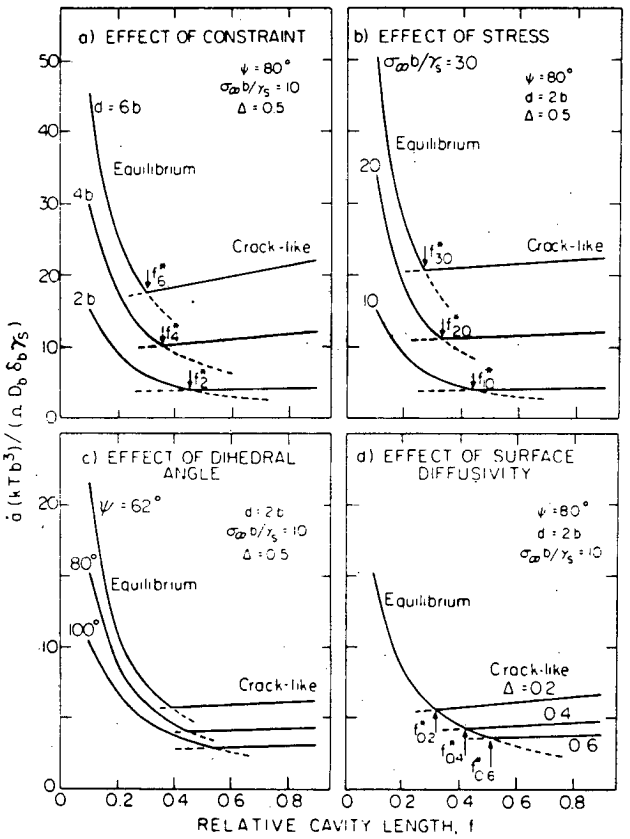

XBL8010-6160

Fig. 15. Trends in the cavity velocity with cavity length.

$$J_s = \dot{V}_o/2\Omega \quad , \tag{40}$$

and that the matter removed from the cavity tip must be deposited on the grain boundary, in order to satisfy matter conservation,

$$\dot{V}_o \approx \dot{\delta}\ell/2 \quad , \tag{41}$$

the boundary 'thickening' rate becomes;

$$\dot{\delta} = 8 \sin(\psi/4)\dot{a}_{crack}^{2/3}(D_s\delta_s\Omega\gamma_s/kT\ell^3)^{1/3} \quad . \tag{42}$$

Combining Eq. (42) with the relations for the boundary transport problem (Eq. (34)) and for the upper bound local constraint (Eq. (9)) permits the cavity velocity to be derived. The velocity is given by [5];

$$\nu^{2/3}\xi^{1/3}[(2/3)(1-f)^3 + (16\sqrt{3}/7\pi)] + 2\nu^{1/3}(1-f)\xi^{-1/3}$$

$$= (3/4)\sigma_\infty\ell/\gamma_s \sin(\psi/4) \quad , \tag{43}$$

where

$$\nu = \dot{a}_{crack}(kT\ell^3/D_b\delta_b\Omega\gamma_s) \quad \text{and} \quad \xi = D_s\delta_s/D_b\delta_b \quad .$$

For situations of practical interest,

$$\sigma_\infty\ell/\gamma_s \sin(\psi/4) \geq 1 \quad .$$

Hence, Eq. (43) reduces, for this highly constrained situation, to,

$$\nu_c^{2/3} \approx 0.15[\sigma_\infty\ell/\gamma_s \sin(\psi/4)]\ \xi^{-1/3} \quad . \tag{44a}$$

An almost constant velocity is thus anticipated in the crack-like region during the highly constrained initial state of cavitation. However, when the constraint is reduced in the later stages of cavitation, cavity acceleration is anticipated, and the cavity velocity attains an unconstrained level given by;

$$\nu_u^{2/3} \approx (3/2)\ [\sigma_\infty\ell/\gamma_s \sin(\psi/4)]\ (1-f)^{-3}\ \xi^{-1/3} \quad . \tag{44b}$$

At very low stress levels ($\sigma_\infty\ell/\gamma_s \sin(\psi/4) \ll 1$), the unconstrained cavity velocity, given by,

$$\nu_u^{1/3} \approx (3/8)\ [\sigma_\infty\ell/\gamma_s \sin(\psi/4)]\ (1-f)^{-1}\ \xi^{-1/3} \quad . \tag{44c}$$

exhibits a stronger stress dependence ($v_u \propto \sigma_\infty$). But, this regime is not likely to be encountered in most practical situations. The trends in the cavity velocity predicted by the above analyses are plotted in Figs. 14a and 15, and the local stress is plotted in Fig. 14b. The transition between the equilibrium and crack-like morphologies is considered favorable when the crack-like velocity exceeds that for equilibrium cavities, and the local stress is assumed to adjust to the crack-like value, over the transition range (Fig. 14b).

The important trends in cavity velocity are illustrated in Fig. 15. Firstly, the strong influence of the constraint upon initial cavitation is noted (Fig. 15a). The effect is manifest at the very earliest stages of cavity growth and continues to be amplified as the extension proceeds. The magnitude of the applied stress (Fig. 15b) also has a substantial effect on the cavity velocity, over the entire range.

The material parameters with the dominant influence upon inhomogeneous cavitation are the local values of the dihedral angle, ψ (Fig. 15c), and the ratio ξ of the surface to boundary diffusivity (Fig. 15d). Smaller values of these quantities encourage cavitation. This may account for the observation that crack-like cavities exhibit relatively small dihedral angles (Fig. 16).

The time t_p taken for cavities to extend across grain interfaces can be deduced from the cavity velocities using,

$$t_p/\ell = \int_{f_o}^{f^*} \frac{df}{\dot{a}_{eqm}} + \int_{f^*}^{f} \frac{df}{\dot{a}_{crack}} \quad . \tag{45}$$

Some typical propagation times for highly constrained cavitation are plotted in Fig. 17. When the dihedral angle or the local surface diffusivity are small and/or the stress is relatively large, most of the time required to develop a full facet length cavity is dominated by the growth in the crack-like mode (as might be anticipated from the velocity diagrams). The initial cavitation that occurs in local regions of a creeping polycrystal (due to small local values of ψ or D_s) can thus be approximately characterized for <u>highly constrained</u>, localized cavitation by a constant cavity velocity, whereupon the propagation time (except at impracticably low stresses, $\sigma_\infty \ell/\gamma_s \sin(\psi/4) < 1$) becomes;

$$t_p^c \dot{\varepsilon}_\infty \approx 50\, \pi(\gamma_s/\sigma_\infty \ell)^{1/2} \sin(\psi/4)^{3/2} \xi^{1/2} \quad . \tag{46}$$

The equivalent propagation time, for uniform <u>unconstrained</u> cavitation is dominated (for most practical <u>stress levels</u>) by equilibrium cavity growth (Eq. (38d)), and given ($\sigma_\infty >> \sigma_o$) by;

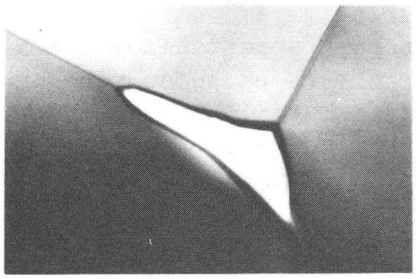

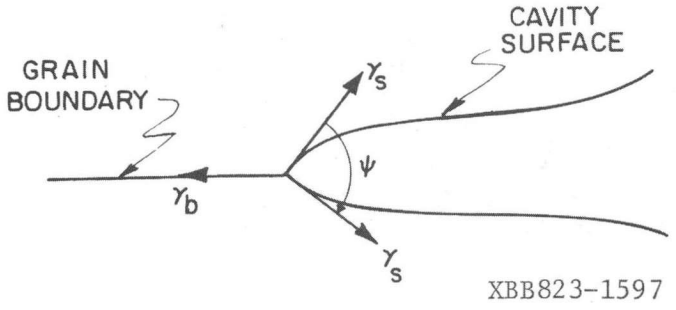

Fig. 16. A transmission electron micrograph of a crack-like cavity in Al_2O_3.

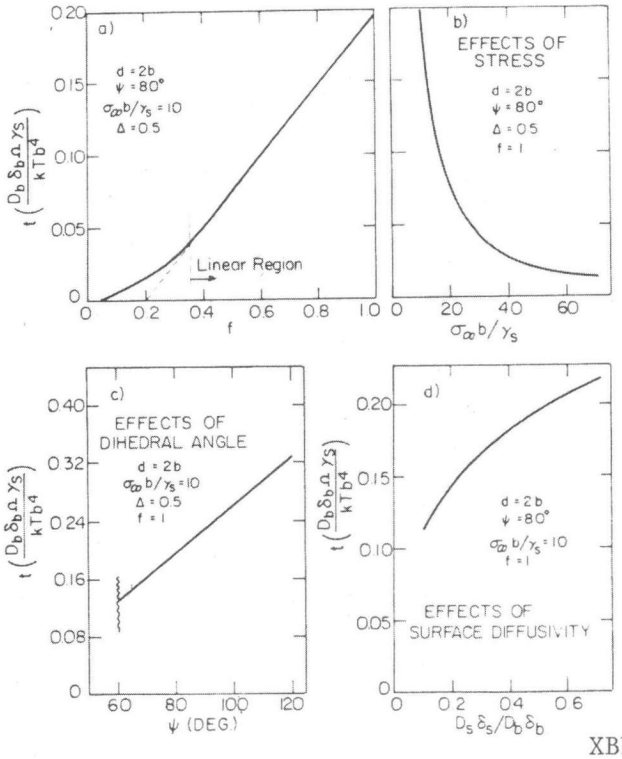

Fig. 17. Cavity propagation times plotted as a function of (a) cavity length, (b) stress, (c) dihedral angle and, (d) diffusivity ratio.

$$t_p^u \left(\frac{\sigma_\infty \Omega D_b \delta_b}{kT\ell^3} \right) \approx \frac{F(\psi)}{80\sqrt{3}} \left[1 - 10 f_o^2 \right] , \qquad (47)$$

where f_o is the initial cavity size (a_o/ℓ). The full-facet cavities, once formed, exhibit a thickening rate, $\dot{y}$, given by [4];

$$\dot{y} = \frac{3D_b \delta_b \Omega}{kTb^2 \lambda [1-\lambda+\lambda^2/\xi']} \left\{ \frac{\sigma_\infty}{(1-\lambda)} - \frac{\gamma_s \tan(\psi/2-\pi/3)}{b\lambda} \right\} , \qquad (48)$$

where 2b is the spacing between neighboring full facet cavities and $\lambda = \ell/b$.

(b) Coarse-grained materials

In coarse-grained ceramics, cavity nucleation on two grain interfaces becomes more prevalent [22] (Fig. 12). The source of these cavities has not been studied. Analogy with metallic systems [17] would suggest nucleation at grain boundary precipitates, especially on sliding boundaries. However, in sintered coarse-grained materials, the remnant porosity during final stage sintering occurs primarily along two grain interfaces (Fig. 18). The cavities in ceramics could thus be equally plausibly associated with fine residual pores. Cavity nucleation at grain boundary ledges that impede sliding (Fig. 19) is another possibility [24]. This issue requires resolution, because the spacing between cavity sites, b, has a profound influence on the cavity growth rates.

The cavities on two grain interfaces also exhibit equilibrium, crack-like and full-facet growth morphologies, but with different geometric characteristics [21] than the cavities at three-grain edges. However, the method of analysis essentially duplicates that described for cavities on three grain corners and hence, only the pertinent cavity growth expressions are presented. Of primary interest are the times required to coalesce adjacent cavities (spacing b) and thereby, to create a full-facet cavity. The principal difference between the full-facet cavity formation times for cavities on two and three grain interfaces resides in the interchange between the cavity spacing b and the grain facet length, ℓ (the effective cavity spacing for three grain edge cavities). The geometric effects also result in important differences for equilibrium cavities at small dihedral angles ($\psi \sim \pi/3$). Otherwise the results generally deviate by less than an order of magnitude. For stress levels at which equilibrium cavity growth dominates, $\sigma_\ell a/\gamma_s < 1.9(1+\xi b/a)$, the coalescence times (subject to the constraint derived from Eq. (10), with $a = \ell$) are given (for $\sigma_\infty >> \sigma_o$) by [10,21];

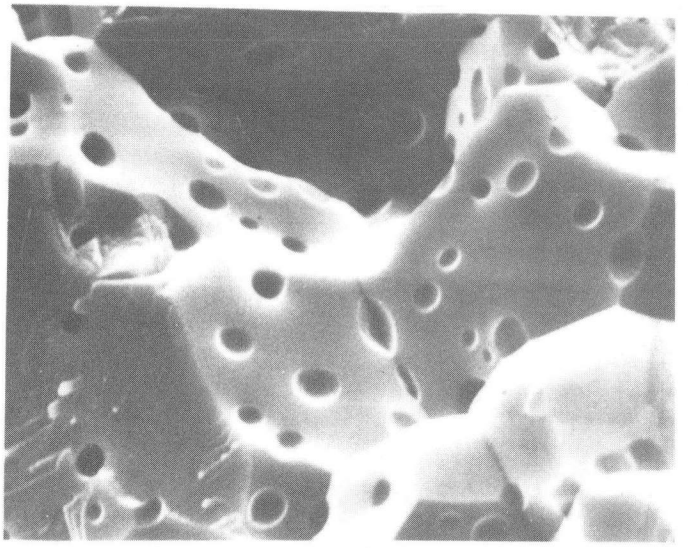

Fig. 18. A scanning electron micrograph of remnant porosity on two grain interfaces in MgO. (XBB823-1952)

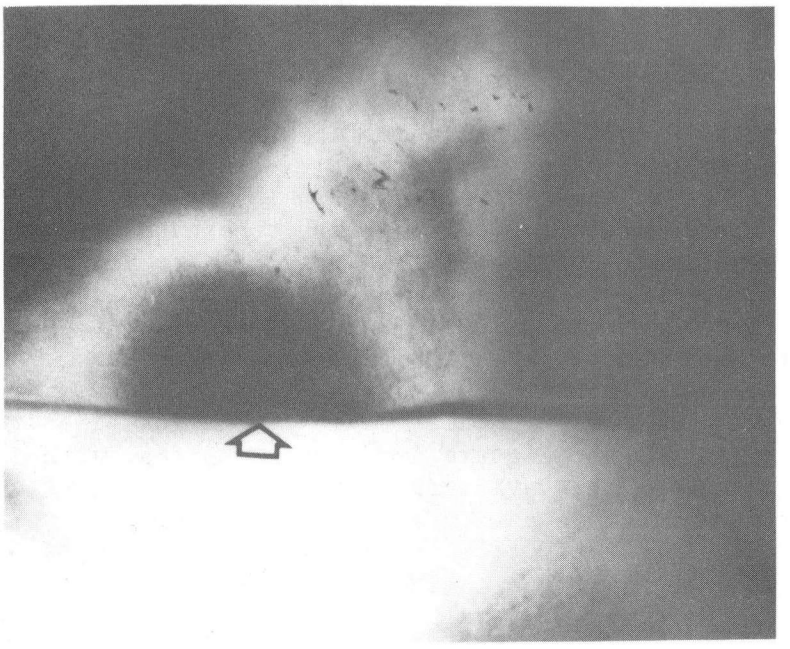

Fig. 19. A transmission electron micrograph of strain contours in the vicinity of a grain boundary sliding impediment in Al_2O_3 (courtesy of J. Porter). (XBB823-1953)

$$t_p^c \dot{\varepsilon}_\infty \approx (2\pi/3)\left[1-(a_o/b)^3\right] g(\psi)\,(b/\ell) \quad ,$$

$$\frac{t_p^u \sigma_\infty \Omega D_b \delta_b}{kTb^3} \approx 0.07\left[1-(a_o/b)^2\right]^3 g(\psi) \quad , \qquad (49)$$

where, $g(\psi) = \text{cosec}(\psi/2)[(1+\cos\psi/2)^{-1}-(1/2)\cos\psi/2]$.
Crack-like cavity growth has not yet been analyzed under constrained conditions. However, in the absence of constraint, at stress levels of most practical concern ($\sigma_\infty b\xi/\gamma_s \sin(\psi/4) > 10$) the coalescence time due to crack-like growth is given by [21];

$$\frac{t_p^u \sigma_\infty^{3/2} D_b \delta_b \Omega}{kT\gamma_s^{1/2} b^{5/2}} \approx 0.33\,\xi^{1/2}\sin^{3/2}(\psi/4)\,H(a_o/b) \quad , \qquad (50a)$$

where,

$$H(a_o/b) = [1-a_o/b]\left\{1-(a_o/b)(1+a_o/b)\left[19-16(a_o/b)-5(a_o/b^2)\right]/16\right\}$$

while at very low stress levels ($\sigma_\infty b\xi/\gamma_s \sin\psi/4 < 1$), cavity coalescence in the crack-like mode occurs within a time [21];

$$\frac{t_p^u \sigma_\infty^3 D_b \delta_b \Omega}{kT\gamma_s^2 b} \approx 3.6\,\sin^3(\psi/4) H(a_o/b)\xi^{-1} \quad . \qquad (50b)$$

Several remarks concerning the latter results are appropriate at this juncture. Similar expressions describe unconstrained crack-like cavity growth from three grain edges in fine grained materials (as derived from Eq. (44b) and (44c) respectively); but these expressions were not presented in the preceding discussion because, in that case, they do not appear to describe a behavioral realm of practical significance. The practical utility of Eq. (50) has yet to be adequately assessed. Nevertheless, the stress dependences provided by these growth processes are of interest. The non-linearity, which arises from a stress dependent cavity width (and extends into descriptions of constrained crack-like cavity growth, as evidenced by Eq. (46)) has been invoked [25] as a source of non-linear rupture behavior observed in the presence of (intrinsically linear) diffusive cavity growth mechanisms. However, some caution must be exercised, by recognizing the limited local stress conditions that must obtain when these modes of cavity growth operate. This issue will be more extensively addressed in a subsequent section.

(c) Finger-like growth

Cavities propagating in the crack-like mode are capable of attaining velocity levels at which the cavity tip becomes unstable in the presence of small perturbations [26]. Subsequent cavity growth then proceeds at an accelerated rate by the growth of finger-like entities from the cavity front (Fig. 20). Analysis of this instability at the tip of a crack-like cavity provides information pertinent to the wavelength, λ_c, of the fastest growth disturbance [26];

$$\lambda_c \approx 2\pi \left(\frac{\gamma_s \Omega D_b \delta_b}{kT\dot{a}}\right)^{1/3} \xi^{-1/6} \quad . \tag{51}$$

Presumably, therefore, a crack-like cavity is capable of developing instabilities when λ_c is appreciably smaller than the total length, z, of the cavity front, e.g., when $\lambda_c \lesssim z/10$. Hence, for cavities emanating from three grain corners, with a cavity front length $z \approx \ell$, insertion of the highly constrained cavity velocity from Eq. (44) into Eq. (51) suggests that finger-like cavities develop when the grain facet length exceeds a critical value, ℓ_c, given by;

$$\ell_c \sigma_\infty / \gamma_s \sin(\psi/4) \gtrsim 5.10^3. \tag{52}$$

Inserting some typical values for creep loading of ceramic materials ($\sigma_\infty \approx 10^8$ Pa, $\gamma_s \approx 1$ Jm^{-2}) indicates that finger-like growth under highly constrained conditions is unlikely in fine grained materials ($\ell < 5$ μm) but probable in more coarse grained polycrystals.

Less stringent limitations on finger formation obtain for unconstrained conditions, because the cavity velocity becomes unbounded as $f \to 1$. For this case, the transition to finger-like growth occurs when;

$$\ell_c \sigma_\infty / \gamma_s \sin(\psi/4) \gtrsim 5.10^2 (1-f)^3 \quad . \tag{53}$$

Hence, finger-like growth should be observed, under unconstrained conditions, even in very fine grained materials ($\ell \sim 1$ μm), when the cavity size $f > 1/2$. The observation of finger-like entities should thus provide an indication of locally unconstrained cavitation.

2.3.2 Materials with a continuous amorphous phase

The critical stress levels for hole formation within an amorphous phase at three and two grain channels (Eqs. (18) and (19)) provide the basis for interpreting and predicting high temperature failure in liquid phase sintered ceramics [15]. At stress levels below the stress needed to nucleate holes at three grain channels, no known failure mechanism exists and the material should deform continuously, without failure, by a

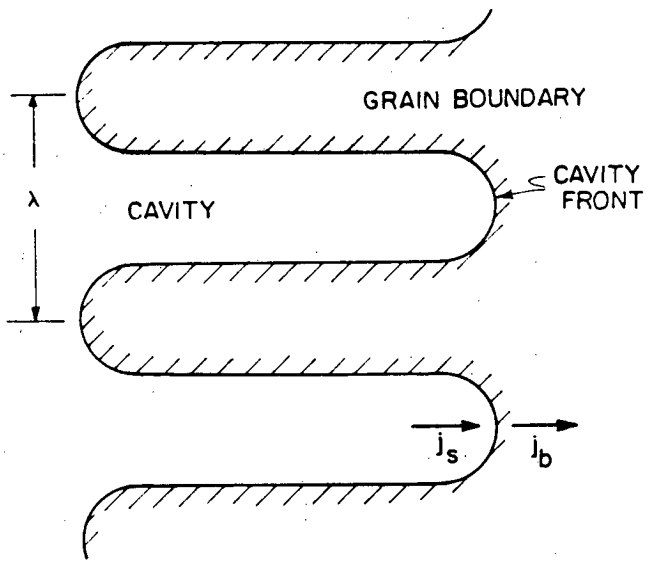

Fig. 20. A schematic of finger-like cavity growth.
(XBL822-5269)

solution/reprecipitation mechanism [27]. The lower critical stress thus constitutes a failure threshold. The practical utility of this threshold is dictated by the magnitude of the tensile stress concentrations that develop at three grain channels, in response to grain boundary sliding and grain rotation. Any tendency toward local dilation by a combination of sliding and rotation substantially enhances the tension within the amorphous pockets and inevitably nucleates holes [28]. However, the detailed analyses (of sliding, viscous flow and solution/reprecipitation that accompany deformation in these materials) needed to compute the magnitude and duration of the stress concentration have yet to be performed. The existence of a practical threshold will thus be regarded an ambiguous issue until further theoretical and experimental work has been conducted. Nevertheless, it is interesting to note that abrupt grain boundary sliding events introduce highly transient tensile stress concentrations (Fig. 11) that are relieved by viscous flow within the pocket and that the net hydrostatic stress within symmetric pockets (Fig. 21a) is zero [18]. Net dilational stresses only occur in certain assymetric pockets (Fig. 21b). The resultant stress duration is dictated by the rate of flow of amorphous material from the neighboring two grain channels. The morphology of the amorphous pockets and the thickness of the two grain channels thus exert an important influence on the failure threshold.

At stress levels above that needed to nucleate holes within two grain channels (Fig. 10, Eq. (19)), facet-sized cavities can develop by the growth and coalescence of the oblate holes within the channel (Fig. 22a). The specific hole growth rate can be computed from standard expressions for the pressure distribution that develops within a parallel sided channel containing a flowing viscous fluid [29];

$$\nabla^2\sigma = 12\eta\dot{\delta}/\delta^3 \quad , \tag{54}$$

where δ is the thickness of the fluid channel. When the fluid perfectly wets the solid (as required for liquid phase sintering) and contains an array of holes with spacing 2b and radius a, the boundary conditions needed to solve Eq. (54) can be specified as follows: symmetry at the mid position between holes requires that $d\sigma/dr = 0$ at $r = b$ (r is the distance from the center of the hole) and chemical potential continuity at the hole surface demands that $\sigma = \gamma_s(1/a + 2/\delta)$ at $r = a$. Then, imposing volume conservation;

$$V_\ell = \delta(2\sqrt{3}\, b^2 - \pi a^2) \quad , \tag{55}$$

where V_ℓ is the fluid volume in the region between prospective cavities, the solution to Eq. (54) can be expressed in terms of the hole growth rate as [15,29];

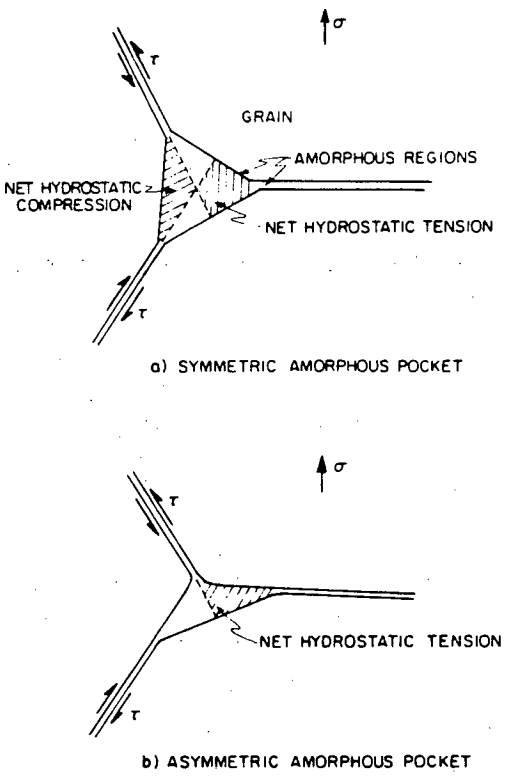

Fig. 21. Schematics illustrating the stressed zones in amorphous pockets induced by grain boundary sliding, (a) a symmetric pocket, (b) an asymmetric pocket. (XBL822-5266)

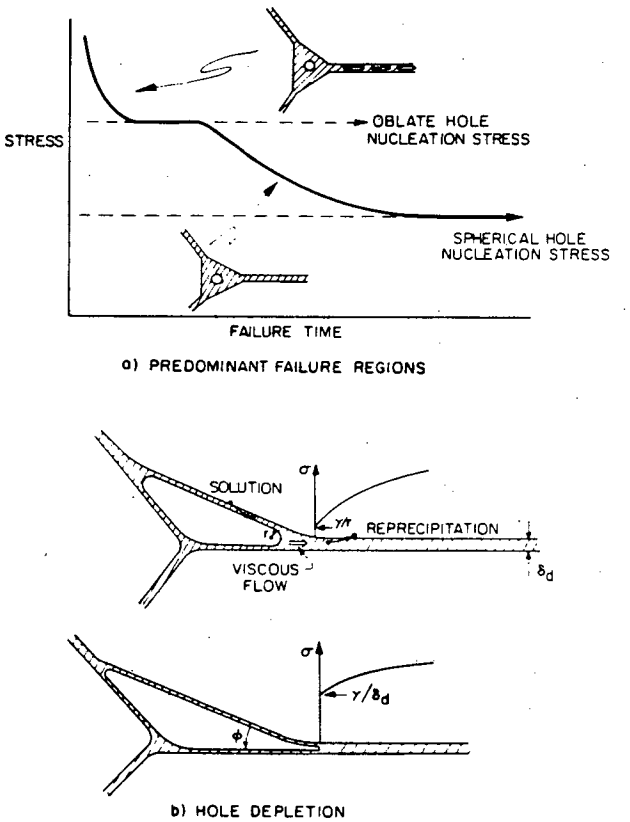

Fig. 22. A schematic of the potential failure processes that can occur in a liquid phase sintered material containing a continuous second phase, (a) general effects of stress, (b) depletion of amorphous pocket.

$$\dot{\alpha} = \left(\frac{\delta_o^2}{5b^2\eta}\right) \frac{(1-0.9\alpha_o^2)\ [\sigma_\ell^i - \gamma_s(1/\alpha b + 2/\delta)(1-0.9\alpha^2)]}{\alpha\ (1.1-\alpha^2)\ [0.96\alpha^2 - \ell n\alpha - 0.72 - 0.23\alpha^4]} \quad , \tag{56}$$

where $\alpha = a/b$ (α_o is the initial value at hole nucleation) and δ_o is the initial channel thickness. The local stress can be deduced by firstly differentiating Eq. (55),

$$\dot{\delta} = \frac{2\pi V_\ell \alpha\dot{\alpha}}{\left(2\sqrt{3}-\pi\alpha^2\right)^2 b^2} \equiv \frac{4\sqrt{3}\pi\delta_o\alpha\dot{\alpha}}{\left(2\sqrt{3}-\pi\alpha^2\right)^2} \quad , \tag{57}$$

and combining with Eq. (7) to obtain (for a boundary normal to the applied stress);

$$\sigma_\ell^i/\sigma_\infty = 1 - 16\sqrt{3}\pi\ \delta_o\alpha\dot{\alpha}/9\ell\left(2\sqrt{3}-\pi\alpha^2\right)^2\dot{\varepsilon}_\infty \quad . \tag{58}$$

Inserting the local stress into Eq. (56) and integrating between α_o and 1 gives the fully-constrained time;

$$t_p^c\ \dot{\varepsilon}_\infty = (8\sqrt{3}/9\pi)\ (\delta_o/\ell)\ T_1^c\ (a_o/b, \sigma\delta_o/\gamma_s) \quad , \tag{59a}$$

where, for the important case $\delta < a_o$,

$$T_1^c = \left[4.6\gamma_s/\sigma_\infty\delta_o - 1\right]^{-1} \left\{ (1.1-\alpha_o^2)^{-1} - 10 + \left[(2.3-\sigma_\infty\delta_o/2\gamma_s\right]^{-1} \ell n \left[\frac{(22-5\sigma_\infty\delta_o/\gamma_s)(1.1-\alpha_o^2)}{1.2+\alpha_o^2-0.5\sigma_\infty\delta_o/\gamma_s}\right]\right\} \quad ,$$

which reduces for $\sigma_\infty\delta_o/\gamma_s \gg 1$ to

$$T_1^c = 10 - \left[1.1 - \alpha_o^2\right]^{-1}$$

or

$$t_p^c\dot{\varepsilon}_\infty \approx \left(\frac{80\sqrt{3}}{9\pi}\right)\left(\frac{\delta_o}{\ell}\right)\left\{1 - 0.1\ \left[1.1-(a_o/b)^2\right]^{-1}\right\} \quad .$$

Note that the hole spacing b has a relatively minor influence on t_p^c (at least when $a_o \ll b$) and that $t_p^c\dot{\varepsilon}_\infty$ increases as δ_o increases. (However, t_p^c may not increase as δ_o increases because $\dot{\varepsilon}_\infty$ may exhibit an inverse dependence on δ_o, e.g., for diffusion limited solution/reprecipitation creep [27]). The equivalent result for unconstrained hole growth is [15];

$$t_p^u \sigma_\infty / \eta = T_1^u(b/\delta_o, a_o/b) \quad , \tag{59b}$$

where T_1^u is the function plotted in Fig. (23).

At stress levels below that required to nucleate holes on two grain interfaces, but above that needed to nucleate holes within amorphous pockets, the first event to initiate during creep rupture is the viscous expansion of the hole within the pocket. This leads to the essential depletion of the pocket (Fig. 22b) by viscous flow of the amorphous phase into the surrounding two grain channels (resulting in an increased film thickness along the two grain interfaces). The process is controlled either by the stress at the hole surface or by the flow rate into the channel. Specific results can be obtained by considering a triangular channel[ii] and rigid displacements of the grain in the direction of the applied stress. Viscous flow along the boundary channel is characterized by the two-dimensional equivalent of Eq. (54);

$$\frac{d^2\sigma(x)}{dx^2} = \frac{-12\eta\dot{\delta}}{\delta^3} \quad . \tag{60}$$

Symmetry requires that $d\sigma/dx = 0$ at the grain facet center ($x=\ell/2$); while the stress at the mouth of the channel ($x=d$) is governed by the stress at the surface of the hole,

$$\sigma(a) \approx \beta\gamma_\ell / r \quad , \tag{61}$$

where r is the radius of curvature of the hole and β ranges between 2 (when the hole is spherical) and 1 (when the hole becomes cylindrical); this stress prevails at the channel mouth provided that viscous flow within the pocket occurs at a sufficiently rapid rate that the stresses in the region between the hole and the channel opening are equilibrated. Integration of Eq. (60) subject to these boundary conditions gives the stress distribution within the channel as;

$$\sigma(x) = \frac{6\eta\dot{\delta}}{\delta^3}\left[(d^2-x^2) + \ell(x-d)\right] + \frac{2\gamma_\ell}{r} \quad . \tag{62}$$

and the separation rate becomes,

$$\dot{\delta} = \frac{\delta^3\left[\sigma_\ell^i - \beta\gamma_\ell(1-2f)/r\right]}{\eta\ell^2\left[1-6f+9f^2-4f^3\right]} \quad , \tag{63}$$

(ii) The channel slope in the presence of complete wetting between the solid and liquid phases must be dictated by anisotropy of the solid/liquid interface energy.

where $f = d/\ell$. The surface tension term, γ_ℓ/r, is of significant magnitude (relative to the local stress) during the two extremes of the depletion process: both immediately after nucleation of the hole and as complete hole depletion is approached. In the presence of stress concentrations (section 2.2) the initial expansion of the cavity occurs rapidly. Hence, it is surmised that the surface tension term does not significantly affect the depletion rate until depletion of the channel is nearly complete (when the surface tension stress increases continuously as the second phase is drawn into the mouth of the two grain interface, Fig. 22b). This process exhibits a relaxation time [15], $\tau_d \approx 2\eta\ell(\tan\phi-\phi)/\sigma_\ell$. Hence, when $t \ll \tau_d$ and the retardation effects that occur in the final stage can be neglected, the time t_d for 'depletion' of the pocket can be expressed directly in terms of the displacements, from Eq. (7) and (63), as ($\gamma_s/r \approx 0$) [15];

$$t_d^c \dot{\varepsilon}_\infty = (4/9)\,(\delta_d-\delta_o)/\ell \quad ,$$

$$t_d^u \sigma_\infty/\eta = \ell^2\,[1-6f+9f^2-4f^3]\,[1/\delta_o^2 - 1/\delta_d^2] \quad , \qquad (64)$$

where δ_d is the thickness of the two grain channel at depletion;

$$\delta_d \approx \delta_o + d^2\tan\phi/2\ell(1-f) \quad ,$$

and ϕ is the angle contained by the triangular pocket (Fig. 22b). The 'depletion' time, t_d, is the time that expires while sufficient material is removed from the pocket that the increase in curvature of the liquid surfaces causes the surface tension stress to increase to a significant fraction of the local stress. It should thus be recognized that a small quantity of residual liquid may remain within the pocket, for a period $t \gg t_d \approx \tau_d$. In fact, the presence of residual liquid, as influenced by the level of the local stress, has a direct association with the next step in the failure sequence: which may occur either by viscous hole extension into the two grain channel or by solution/reprecipitation.

When the local stress after hole depletion exceeds γ_ℓ/δ_d, the liquid meniscus can be drawn into the channel mouth (Fig. 22b), by allowing a positive pressure gradient to be retained within the liquid. Under these conditions, the thickness of the liquid film increases, as the meniscus enters the channel, causing both the stress at the meniscus to decrease and allowing nucleation of holes within the two grain channel (Eq. (19)). A combination of finger-like hole growth from the channel mouth (see Eq. (75)) and expansion of oblate holes (Eq. (59)) then permits full-facet cavitation to proceed at a rate presumably in excess of that attained by solution/reprecipitation.

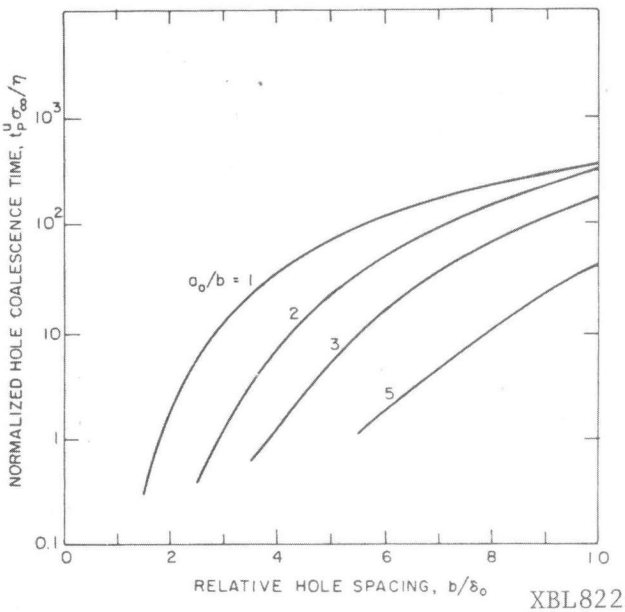

Fig. 23. A plot of the unconstrained hole coalescence time as a function of the initial film thickness for several choices of the hole nucleation size.

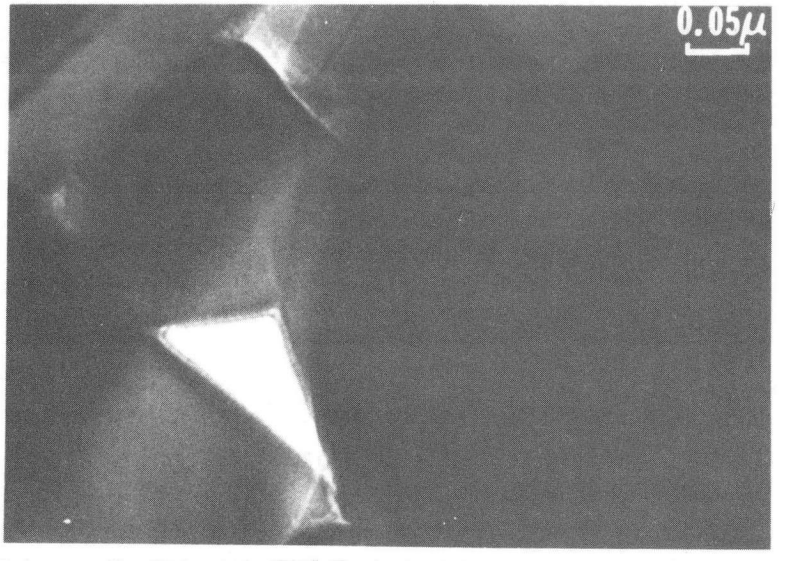

Fig. 24. A transmission electron micrograph of a thin amorphous film over a cavity surface observed in Si_3N_4. (XBB823-1954)

However, when the local stress is not high enough to induce full-facet cavitation by visous flow mechanisms, the depleted holes extend (more slowly), by a solution/reprecipitation process. Solution/reprecipitation is motivated by a stress difference between the liquid film at the cavity surface[iii] and the liquid within the channel, and entails the transport of the solid phase, through the liquid, from the cavity surface onto the grain surfaces within the channel. Hence, further redistribution of the liquid phase is not necessarily involved. The process can be either diffusion controlled or interface controlled; both possibilities will be examined. Before proceeding, it is noted that solution/reprecipitation can occur concurrently with pocket depletion (by viscous flow) and hence, that a rigorous analysis would examine this concurrence. But, for simplicity, solution/reprecipitation is considered to initiate when hole depletion is essentially complete because, for most practical systems, the solution/reprecipitation process is the most time-consuming constituent in full-facet cavitation (as substantiated in the subsequent analysis).

Diffusion controlled solution/reprecipitation requires that a chemical potential gradient exists along the channel to motivate migration of the solid phase. This can only be achieved in the presence of a pressure gradient within the liquid. A suitable pressure gradient exists if the liquid phase continues to flow within the channel, throughout the process; suggesting that viscous flow is a necessary accompaniment to solution/reprecipitation. However, it is also noted that the viscous flow prerequisite may be obviated in the presence of grain boundary ledges that substantially impede viscous flow through the channel. In the absence of an appreciable spatial density of ledge-like impediments, the stress distribution within the channel (Eq. (62)) dictates the mass transport rate along the channel. The specific rate of diffusion is given by the differential equation

$$\frac{d^2\sigma(x)}{dx^2} = -\frac{\dot{kT\Delta}}{\Omega D_\ell C_\ell \delta} , \qquad (65)$$

(iii) The complete wetting requirement for liquid phase sintering suggests that a liquid film is likely to exist over the cavity surfaces, as generally observed (Fig. 24). However, it is emphasized that the complete wetting between solid and liquid required for sintering only specifies a zero dihedral angle pertinent to the liquid along a grain boundary within the solid and does not relate to solid, liquid, vapor equilibrium.

where $\dot{\Delta}$ is the rate of separation of the grain centers induced by matter deposition on the grain surfaces, D_ℓ is the diffusivity of the solid phase in the liquid and C_ℓ is the solubility of the solid in the liquid. Integration of Eq. (65), subject to the same boundary conditions pertinent to viscous flow in the channel, gives;

$$\sigma(x) = \frac{kT\dot{\Delta}}{2\Omega D_\ell C_\ell \delta}\left[(d^2-x^2) + \ell(x-d)\right] + \frac{2\gamma_\ell}{r} \quad . \tag{66}$$

Comparison of Eqs. (62) and (66) indicates that;

$$\frac{\dot{\Delta}}{\dot{\delta}} = \frac{12\Omega D_\ell C_\ell \eta}{kT\delta^2} \quad . \tag{67}$$

This result illustrates that cavity growth by diffusion controlled solution/reprecipitation is likely to proceed most rapidly when the liquid film thickness is small, contrary to intuitive expectations (a tendency that will not, of course, apply when appreciable ledge-like impediments exist along the grain interfaces). Additionally, solution/reprecipitation cavity growth is encouraged by a high diffusivity (as expected) and a high liquid viscosity. Combining Eqs. (7), (63), and (67) and recognizing that the local stress (Eq. (7)) is dictated by the sum, $\dot{\delta} + \dot{\Delta}$, the differential equation describing the grain separation rate due to matter deposition can be derived as,

$$\dot{\Delta}(t)\left\{\frac{\ell^2 kT\left[1-6f(t)+9f^2(t)-4f^3(t)\right]}{12\Omega D_\ell C_\ell \delta(t)} + \frac{4\sigma_\infty}{9\dot{\varepsilon}_\infty}\left[1 + \frac{kT\delta^2(t)}{12\Omega D_\ell C_\ell \eta}\right]\right\}$$

$$= \sigma_\infty - \beta\gamma_\ell(1-2f)/r \quad . \tag{68}$$

Cavity growth is controlled in this instance by the rate of transport of the solid phase through the liquid that exists within the two grain channel and along the cavity surface. Specifically, domination of the cavity growth rate by diffusion through the liquid over the cavity surface, vis-a-vis diffusion along the channel, is presumed to be dictated by the relative film thickness, δ_s/δ_b, at the two locations (the role of δ_s/δ_b being analagous to that of the diffusivity ratio $D_s\delta_s/D_b\delta_b$ in the previously discussed cavity growth problem for single phase systems). However, for the present problem, the requirements on the contained angle, ϕ, are not readily specified and an exact solution for the cavity growth rate awaits further consideration of this issue. Several simplifying assumptions (concerning the trends in ϕ with cavity expansion) can, of course, be made in order to obtain preliminary solutions. In this context, it is tempting to propose that diffusion through the

fluid film over tne cavity surface is rapid enougth to maintain a constant contained angle, ϕ, during cavity growth. However, this assumption yields an inadmissible solution for unconstrained cavity growth; as well as being at variance with available observations (Fig. 25), which suggest that ϕ decreases as the cavity expands. Instead, the observations are used to suggest the assumption that the cavity only extends along the boundary normal to the applied stress and does not progress along the inclined boundaries. Then, volume conservation of the solid phase (the liquid phase volume is necessarily constant) permits Δ to be expressed as;

$$\dot{\Delta} = \ell f_o \dot{f} \quad . \tag{69}$$

A solution for t_p can, in principle, be obtained by combining Eqs. (63), (68) and (69). However, the solutions are unwieldy. Hence the only results presented herein pertain to the case, $\dot{\Delta} >> \dot{\delta}$ (as dictated by Eq. (67)) and for $\sigma_\infty >> \gamma_s/r$; the implied loss of driving force (that accompanies an increase in δ) and neglect of the stress at the channel mouth results in lower bound cavitation times;

$$t_p^c \dot{\varepsilon}_\infty > (2/9)\,(d_o/\ell)\,[1-2d_o/\ell] \quad , \tag{71}$$

$$t_p^u \sigma_\infty \left(\frac{C_\ell D_\ell \delta_\ell \Omega}{kT\ell^3}\right) > (1/192)\,(d_o/\ell)$$

$$\{1-16(d_o/\ell)+48(d_o/\ell)^2-48(d_o/\ell)^3+16(d_o/\ell)^4\} \quad .$$

The constrained time t_p^c (being insensitive to the atom transport rate) can be expected to exceed the lower bound by up to ~2, (as obtained when $\dot{\delta} \approx \dot{\Delta}$); while the unconstrained time could be substantially in excess of the lower bound.

Cavity growth by solution/reprecipitation could be interface limited [27]. Then, the stress within the liquid layer at the grain interface can equilibrate at the level of the locally applied stress; except near the cavity tip where the stress must decrease to ~0 as the cavity surface is approached. Assuming that the stress gradient with the liquid can be supported by fluid flow into the channel mouth and over the cavity surface, the matter deposition rate along the grain interface is simply;

$$\dot{\Delta V}_{int} = \sigma_\ell \Omega k_1 \ell(\ell-d)/kT \quad , \tag{72}$$

where k_1 is the rate of condensation of atoms from the liquid film onto the grain surface: a parameter that can be determined from crystallization or creep studies [27]. Then, subject to volume conservation (Eq. (69)), the cavitation time for equilibrium shaped cavities, when $\dot{\Delta} >> \dot{\delta}$, becomes,

$$t_p^c \dot{\varepsilon}_\infty = (2/9)\,(d_o/\ell)\,[1-2d_o/\ell] \quad ,$$

$$t_p^u \sigma_\infty k_1 \Omega/kT = \ell[1-(d_o/\ell)] \quad . \tag{73}$$

Note that the constrained result is necessarily the same as that for the diffusion controlled process.

Comparison of the cavitation times for each of the prospective processes suggests that, under fully-constrained conditions (when only the cavity morphology and matter conservation requirements are important) the cavitation times are similar for all processes; with distinctions between mechanisms depending on specific hole spacings, pocket shapes and sizes, film thicknesses etc. Some typical choices for liquid phase sintered Si_3N_4 (Table I), indicate that the

Table I

Constrained Processes for Si_3N_4

$\delta_o \approx 20\text{Å}$, $\ell \sim 1\ \mu m$, $d_o \sim 0.1\ \mu m$

Process	$t^c \dot{\varepsilon}_\infty$
Oblate Hole Coalescence	$\sim 10^{-2}$
Pocket Depletion	$\sim 5 \times 10^{-3}$
Solution/Reprecipitation	$\sim 2 \times 10^{-2}$

fastest constrained process for this material is pocket depletion, while solution/reprecipitation is the slowest. This is consistent with the frequent observation of both hole depletion (Fig. 24) and of cavity expansion by solution/reprecipitation (Fig. 25), and the infrequent detection of holes along two grain interfaces (Fig. 9). When the constraint relaxes, during subsequent cavity growth, appreciably different cavitation rates can be attributed to

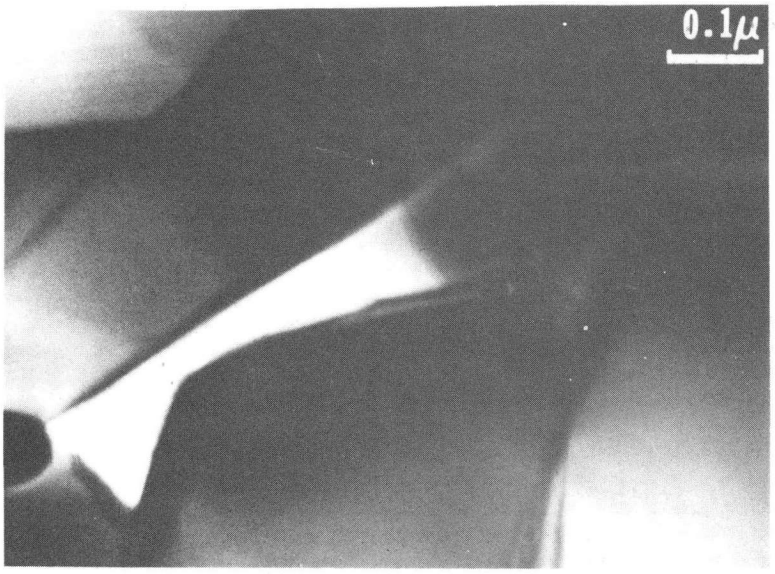

Fig. 25. A transmission electron micrograph of a cavity in Si_3N_4 extended by solution/reprecipitation.
(XBB823-1955)

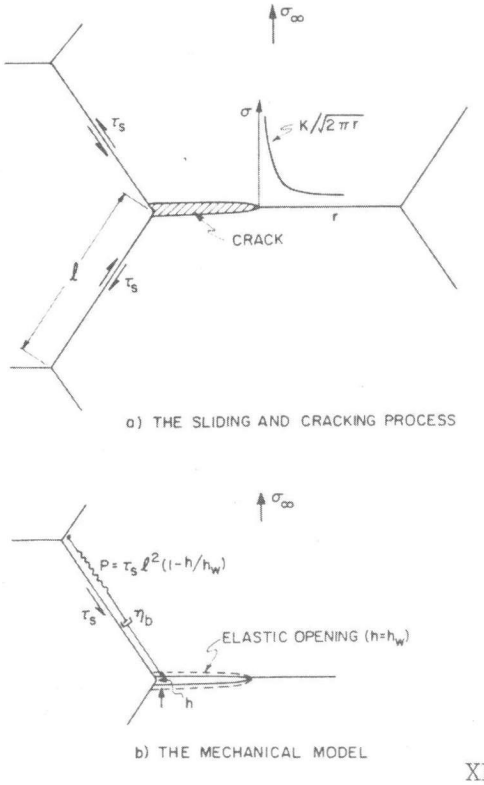

XBL822-5271

Fig. 26. A schematic of the grain boundary sliding and brittle cracking process, (a) the stress field, (b) the mechanical model.

the various growth mechanisms, depending primarily on the viscosity of the amorphous phase and the diffusivity of the solid in the liquid.

Finger-like hole growth can also initiate within the amorphous layer at high hole growth rates. The critical wavelength for this process is given by;

$$\lambda_c = \pi \left(\frac{\gamma \delta^2}{3\eta \dot{a}} \right)^{1/2} . \tag{74}$$

For unconstrained growth of a hole, by viscous flow, from a three grain corner, finger-like growth will occur when;

$$\frac{\sigma_\infty \ell}{\gamma (1-f)^4} \tilde{>} \pi^2/4 . \tag{75}$$

2.3.3 The role of grain boundary sliding

Brittle cracking or cavity growth along grain boundaries, motivated by the sliding of neighboring grain boundaries, may occur during creep (Fig. 26a). However, this process is confined to the limited set of situations for which appreciable mass transport by diffusion or viscous flow is prohibited [30]; because grain boundary and surface diffusion modify both the surface profile [20] and the stress state ahead of the crack and thereby create a diffusive cavity that propagates in accord with the mechanisms described in the preceding sections (with grain boundary sliding as an incidental, rather than a motivating, process, c.f. diffusive creep [12]). When significant diffusion or viscous flow is not admitted, and the only permissable viscous motion occurs by grain boundary sliding, brittle cracks are tenable. The occurrence of this condition must be limited (since grain boundary sliding itself usually involves diffusive processes [12], because of the presence of ledges and of nonplanarity). Nevertheless, important situations can be conceived wherein the proposed process might be encountered. For example, ceramics prepared by liquid phase sintering (e.g., Si_3N_4) often have planar boundaries, and contain a second phase at the boundaries that is too narrow (a few lattice spacings, Fig. 8) to admit significant viscous modifications of the crack tip[iv], but wide enough to facilitate boundary sliding.

If diffusion or viscous flow are excluded, grain boundary sliding will result in elastic stress concentrations at grain triple points. The stress concentration (in the absence of dislocation plasticity) has the square root singularity

---

[iv] The brittle cracking in this instance refers to fracture of the thin amorphous phase in a manner analagous to the fracture of liquids.

dislocation plasticity) has the square root singularity typical of shear cracks [30]. A crack will develop from the triple point either if the singularity attains the critical level required for grain boundary (or second phase) fracture, $K_c^{g\cdot b}$, or if a defect of sufficient size pre-exists at the grain boundary. The onset of cracking will thus depend on the local conditions at individual triple points.

The presence of the crack will relax the elastic stress concentration at the triple point and permit the adjacent boundaries to slide; thereby producing an opening displacement at one end of the crack. As the sliding progresses, the stress intensity factor at the micro-crack tip (Fig. 26a) increases, causing additional crack extension and further sliding. Also, the stress concentration at the neighboring triple points becomes enhanced, leading to an increased probability of microcrack initiation at these locations. Once the crack reaches the opposing triple point, the singularity at its tip will begin to relax, by sliding of the intersecting boundaries, and further crack extension will be suppressed. The ultimate formation of open facet-sized cracks is thus to be anticipated. Failure will presumably occur when sufficient contiguous boundaries have developed cracks (forming a macrocrack of critical size) [31]. The interaction of propagating cracks with performed cracks is thus undoubtedly involved in the failure process.

The extension of a wedge crack the emanates at a triple point can be analyzed using a cracked dislocation solution, [30,32]

$$K \approx \sigma_n\sqrt{\pi(a/2)} + hE/\sqrt{2\pi a}(1-\nu^2) \quad , \qquad (76)$$

where 2h is the wedge opening, a is the crack length, K is the stress intensity factor, E is Young's modulus and σ_n is the component of the applied stress normal to the crack. The first term is due to the normal opening of the crack and the second derives from the wedge opening produced by sliding.

A crack will propagate whenever the stress intensity factor K exceeds the critical value $K_c^{g\cdot b}$. The motion of a crack on a susceptible boundary can thus be directly obtained from Eq. (76) once the time dependence of the opening h has been established. The resultant crack propagation exhibits the general characteristics depicted in Fig. (27). The initial growth is constrained by the grain boundary sliding rate. However, when the crack reaches a critical length a*, at which it can continue to propagate at a fixed wedge opening h* (due to the action of the normal stress, σ_n), the constraint imposed by the boundary sliding rate becomes relaxed and the crack will extend catastrophically up to the stable length ℓ. The propagation time t_p is determined by the time taken for the crack to attain the critical length a*. Hence, t_p can be ascertained if both a* and the driving force for sliding in the range $0 < a < a^*$ can be deduced.

The critical length a* is given by the coupled requirement that K increases with crack length at a fixed wedge opening h, i.e., the crack is driven by the normal stress, and that K at this condition, K*, is equal to $K_c^{g \cdot b}$. The first condition is established by determining when K, for a fixed h, is a minimum; because, upon exceeding the minimum, K will increase monotonically with crack length and the crack will become unstable. Hence, differentiating Eq. (76) with respect to a at fixed h and setting to zero, gives

$$a^* = h^* E/\sigma_n \pi(1-\nu^2) \quad . \tag{77}$$

Substituting h* from Eq. (77) into Eq. (76), and requiring that the resultant $K = K_c^{g \cdot b}$, then gives;

$$a^* = \frac{1}{2\pi}\left(\frac{K_c^{g \cdot b}}{\sigma_n}\right)^2 \quad . \tag{78}$$

The rate of wedge opening $\dot{h}$ is determined by a conventional spring, dashpot approach; wherein the opening is motivated by the elasticity of the material and resisted by the viscosity η_b of the sliding boundary (Fig. 26b). The wedge opening permitted by the elasticity of the material is governed exclusively by grain boundary sliding and therefore relates to the resolved shear stress τ_s. The normal stress is not involved because it generates an opening at the crack center but not at the wedge. The problem is most conveniently posed using the illustration shown in Fig. 26b. The wedge crack releases the constraint of the surrounding grains on the triple point and the grain on one side of the sliding boundary exerts an elastic force on the triple point. As the crack extends and the wedge opening increases the force decreases, and must reduce to zero at elastic equilibrium, i.e., at the stable value of the elastic wedge opening, h_w (Fig. 26b). The reduction in force occurs in accord with the linear elastic properties of the grain, such that the average effective shear stress τ_B acting on the boundary at any instant is

$$\tau_B = \tau_s(1 - h/h_w) \quad . \tag{79}$$

But, the average sliding rate $\langle \dot{u} \rangle$ can be related to the average effective stress τ_B by:

$$\langle \dot{u} \rangle = \tau_B \delta_b/\eta_b \equiv (\tau_s \delta_b/\eta_b)(1 - h/h_w) \quad . \tag{80}$$

Hence, noting that;

$$\langle u \rangle = \frac{\pi}{4} h \operatorname{cosec}\phi \quad , \tag{81}$$

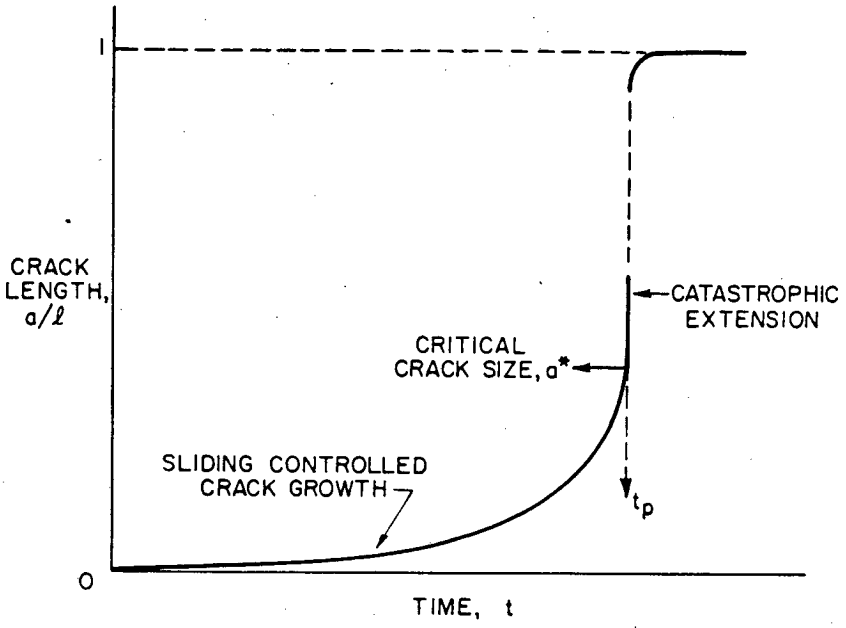

XBL 798-6905

Fig. 27. The growth characteristic of a brittle crack restricted by the sliding rate of the neighboring grain boundary.

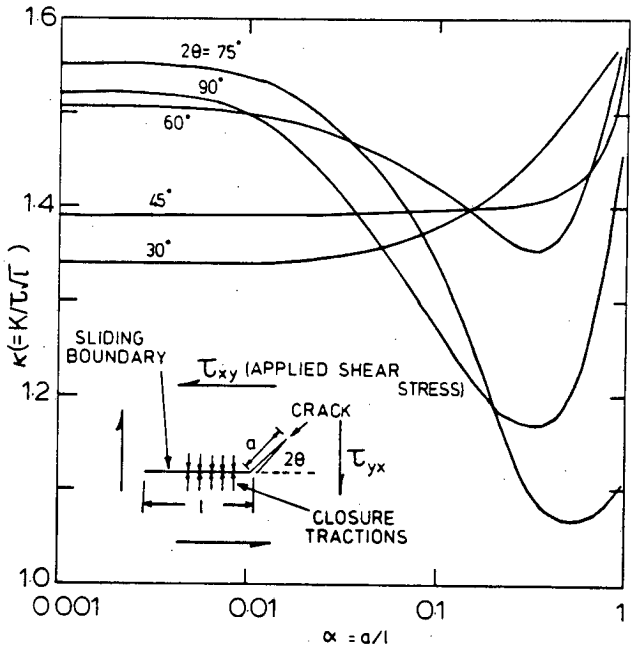

XBL806-10227

Fig. 28. A plot of the normalized stress intensity factor pertinent to grain boundary sliding and brittle cracking.

the wedge opening becomes;

$$\dot{h} = \frac{4 \sin \phi \tau_s \delta_b}{\pi \eta_b} [1 - h/h_w] \quad . \tag{82}$$

The equilibrium elastic opening h_w (at which the elastic driving force is zero) is dictated exclusively by the grain boundary sliding and represents the opening at which sliding would cease. The equilibrium opening will depend on both the instantaneous crack length and the in-plane shear stress [30];

$$h_w = \frac{\sqrt{2\pi}(1-\nu^2)a\tau_s}{E} \left[\frac{\kappa^\tau(a/\ell,\phi)}{\sqrt{a/\ell}} - \sqrt{\pi/2} \sin 2\phi \right] , \tag{83}$$

where κ^τ is plotted in Fig. 28. The instantaneous wedge opening h prior to catastrophic extension is determined by applying the crack extension requirement ($K = K_c^{g \cdot b}$) to Eq. (76), giving

$$h = \frac{\sqrt{2\pi}(1-\nu^2)a}{E} \left[(K_c^{g \cdot b}/\sqrt{a}) - (\sqrt{\pi/2}\ \sigma_n) \right] \quad . \tag{84}$$

Differentiation then yields the opening rate $\dot{h}$, as

$$\dot{h} = \frac{\sqrt{2\pi}(1-\nu^2)\dot{a}}{E} \left[(K_c^{g \cdot b}/\sqrt{a}) - (\sqrt{\pi/2}\ \sigma_n) \right] \quad . \tag{85}$$

Substituting the above results for h, h_w and $\dot{h}$ into Eq. (82) and rearranging gives

$$\dot{a}(1-\nu^2)\left(\frac{\eta_b}{E\delta_b}\right) = \frac{4 \sin\phi\sqrt{a}}{\pi^2} \left\{ \frac{\left[\sqrt{a} - 2\sqrt{a^*} + (\tau_s/\sigma_n)(\kappa\sqrt{2\ell/\pi} - \sqrt{a} \sin 2\phi)\right]}{(\kappa\sqrt{2\ell/\pi} - \sqrt{a} \sin 2\phi)(\sqrt{a^*} - \sqrt{a})} \right\} . \tag{86}$$

The significant features of Eq. (86) to note are: (a) there is a threshold for crack development (obtained by setting the numerator to zero) given by the condition

$$\kappa\tau\sqrt{\ell}\Big|_{a=0} > K_c^{g \cdot b} \quad ,$$

(b) the velocity becomes unbounded as $a \to a^*$, (c) the velocity above the threshold condition is zero at a=0. The general trends are complex. However, some conditions wherein simplified crack velocity relations pertain can be explored by re-expressing Eq. (86) in terms of a threshold stress, through the term

$$a^*_{th} \equiv \ell(\tau_s/\sigma_n)^2\kappa^2/2\pi = (\pi/2)(K_c^{g \cdot b}/\sigma_n)^2_{th} \quad , \tag{87}$$

to obtain:

$$\dot{a}(1-\nu^2)\left(\frac{\eta_b}{E\delta_b}\right) = \frac{4\beta \sin\phi (a/a^*)^{1/2}}{\pi^2} \frac{[(a/a^*)^{1/2}(1-\beta \sin 2\phi)+2(a^*_{th}/a^*)^{1/2}-2]}{[2(a^*_{th}/a^*)^{1/2}-\beta(a/a^*)^{1/2}\sin 2\phi][1-(a/a^*)^{1/2}]} , \tag{88}$$

where $\beta = \tau_s/\sigma_n$. For stresses considerably in excess of the threshold, such that $a^* \ll a^*_{th}$ and for β values typical of crack-susceptible boundaries ($\beta \sim 1$), Eq. (88) reduces to:

$$\dot{a}(1-\nu^2)(\eta_b/E\delta_b) \approx 4 \sin\phi\beta(a/a^*)^{1/2}/\pi^2[1-(a/a^*)^{1/2}] . \tag{89}$$

Note that the facet length ℓ does not enter this limit solution.

The time of propagation t_p of a crack across the boundary facet can be obtained by direct integration of the velocity relation. For the limit solution, Eq. (89), the following simple result obtains:

$$t_p = \frac{\pi(1-\nu^2)}{8 \sin\phi} \frac{(K_c^{g\cdot b})^2}{\sigma_s \tau_s} \left(\frac{\eta_b}{E\delta_b}\right) . \tag{90}$$

This result provides useful insights into the relative roles of the important microstructural variables, η, δ_b, $K_c^{g\cdot b}$, ϕ, and of the relative stress conditions σ_n, τ_s. For a uniaxial tension σ_∞ inclined at an angle ψ to the sliding boundary,

$$\tau_s = \sigma_\infty \sin\psi \cos\psi ,$$

$$\sigma_n = \sigma \sin^2(\psi + \phi) ,$$

Equation (90) becomes;

$$t_p = \frac{\pi(1-\nu^2)}{8\sigma_\infty^2}\left[\frac{(K_c^{g\cdot b})^2 \eta_b}{E\delta_b}\right][\sin\phi \sin\psi \cos\psi \sin^2(\psi+\phi)]^{-1} . \tag{91}$$

The non-linear stress dependence is significant: a result that essentially derives from the condition that the crack length at critically a* is proportional to the inverse square of the normal stress. Differentiation of Eq. (91) with respect to ϕ and ψ suggests that the most fracture susceptible boundaries (those with minimum t_p) pertain for the condition $\psi = 35°$, $\phi = 55°$, yielding

$$(t_p)_{min} \approx \left(\frac{K_c^{g\cdot b}}{\sigma_\infty \sqrt{\delta_b}}\right)^2 \frac{\eta_b}{E} \quad . \tag{92}$$

An extension of this analysis to incorporate limited diffusion or viscous flow can be contemplated. In the presence of limited atom transport rates along the cavitating boundary, the neighboring grains can deform in a predominantly elastic manner and a behavior analagous to brittle cracking results. This mode of cavitation is tenable whenever the atom transport rate is small enough to prohibit the rigid separation of grains bordering the cavitating interface. Consideration of relaxation times for grain boundary diffusion over the cavitating facet[(v)], in the presence of elastic deformation, reveals that elastic cavity growth prevails when[21]

$$(\langle\sigma\rangle/G) \gg a/(\ell-a) \quad ,$$

where $\langle\sigma\rangle$ is the average stress between the cavity tip and the adjacent three grain corner. Such behavior only occurs, therefore, at high stress levels (e.g., in the vicinity of a macrocrack tip). When these conditions are satisfied, solutions for the propagation time can be deduced for specific cavity growth mechanisms. This is achieved by invoking a relation between $\dot{a}$ and K characteristic of the operative mechanism (for example, Eq. (112), pertinent to elastically driven cavity growth by grain boundary diffusion) and inserting into an expression for K deduced from Eqs. (76), (82), and (85);

$$K = \sigma_\eta \sqrt{\pi a/2} + \frac{E h_w [1-\exp(-t/\tau_b)]}{\sqrt{2\pi a}(1-\nu^2)} \quad , \tag{93}$$

where $\tau_b = \pi\eta_b h_w/4 \sin\phi\tau_s\delta_b$. Integration of the resultant differential equations yields t_p. However, specific solutions remain to be determined.

(v) A diffusion process confined to the cavitating facet is probably appropriate in the presence of grain boundary sliding.

A simplified procedure for estimating t_p, suggested by Tsai and Raj [28], is based on a constant cavity velocity assumption and a cavity growth rate $\dot{a} \propto K^2$. Applied to viscous hole growth motivated by grain boundary sliding, this procedure yields;

$$t_p \approx 10^{-4}(\ell/\delta_o)^3(En/\sigma_\infty)^2 \quad . \tag{94}$$

2.4 Cavity Coalescence

The ultimate failure of polycrystalline ceramics occurs when facet-sized cavities coalesce to form an identifiable crack, which then extends to a critical dimension. Cavity coalescence is thus an important phase in the high temperature failure process. The coalescence process is sensitively dependent upon the existence of constraint. Two extremes are amenable to analysis and provide a useful basis for the interpretation of experimental results. When the cavities are very narrow, as pertinent either to crack-like cavities or to cavities formed by hole growth (within a thin viscous grain boundary phase) at high local stress levels, the small cavity volume may be elastically accomodated, by the sliding of the contiguous boundaries [31]. Then, the cavities may be regarded as independent statistical entities subject to a stress at the level of the applied stress (Fig. 29). Similarly, when many cavities develop simultaneously along planar zones within the microstructure (as apparently occurs in certain ceramics), the matrix constraint is small (large d in Eq. (10)) and cavity growth independence can again be regarded as an approximately valid basis for analysis. The independent formation of facet-sized cavities, and their coalescence to form a crack, can be treated using standard probabilistic procedures to obtain expressions relating the crack nucleation time to stress and microstructure. The resultant failure time expressions are necessarily specimen-size dependent.

When inhomogeneous cavitation occurs within small microstructural regions (of the order of several grain dimensions) at low stress levels, such that the cavity widths are large enough to exclude elastic volume accomodation, constraint exerts an important influence on the cavity coalescence mechanism [5]. In this instance, the tensile stress concentrations that develop outside the initial cavitation zone induce a zone spreading process along planes normal to the applied stress (Fig. 30). Analysis of the zone spreading conditions provides the basis for predicting specimen-size independent crack nucleation times.

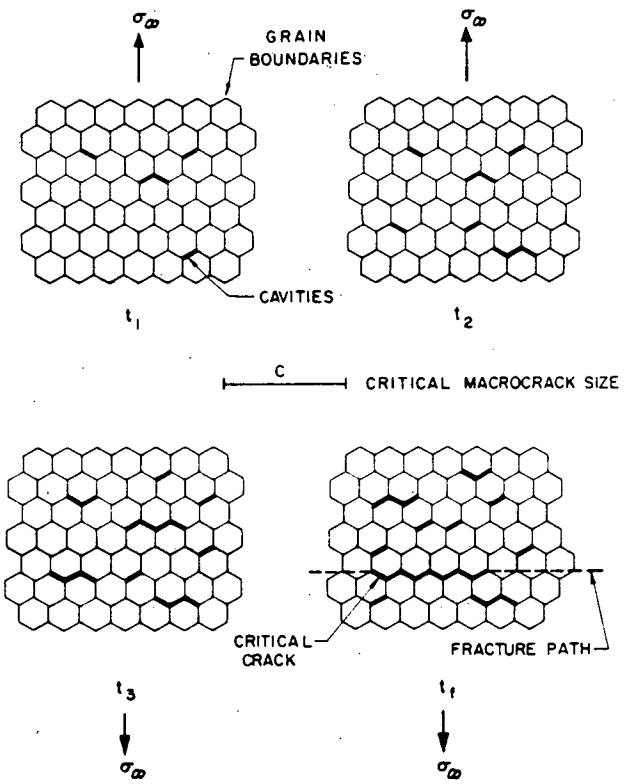

XBL793-5995

Fig. 29. A schematic of cavity coalescence by a statistical accumulation of contiguous cavities.

2.4.1 Probabilistic cavity coalescence

The development of a probabilistic model for the failure time requires that a critical size, a_c, be defined at which a coalesced array of cavities constitutes a macrocrack. This is, in general, a rather nebulous concept, because the critical size depends on the microstructure, and on the size of the crack tip 'process zone' (i.e., the enhanced cavitation zone created by the crack). The zone size depends, in turn, on the level of the applied stress or, more likely, on the stress intensity factor K. The simplest approach capable of yielding useful results is to assume that a macrocrack has developed when K attains a specified level; namely, when K reaches a certain fraction K_f of the critical stress intensity factor K_c. The critical size for a penny-shaped crack can then be written as;

$$a_c = \pi K_f^2 / 4\sigma_\infty^2 \quad . \tag{95}$$

The formation of a macrocrack of size a_c will be determined by the distribution of times, t_p, for the development of facet-length cavities (section 2.3). This time is statistically distributed, because of the variability of grain boundaries with regard to second phase content and composition, boundary energy, diffusivity, etc. It is required for present purposes that a distribution function be assigned to this propagation time; namely, a function that can be expected to accurately describe the grain boundary variability typical of ceramics. This decision is facilitated by noting that only a small fraction of the boundaries usually cavitate prior to failure: these being the boundaries with the greatest cavitation susceptibility. When such conditions pertain, a distribution that characterizes the large extreme of cavitation susceptibilities should apply. There are only three extreme value distributions [31] and therefore the choice of functions can be considerably restricted by applying the extreme value condition. Initially, a distribution based on the second type of extreme value function is selected, because this distribution has previously been found to describe extreme value characteristics of ceramic microstructures [31]. An additional rationale for the chosen distribution is provided later. The assumed cumulative probability, $p(t_p)$ of observing facet sized cavities at time t_p is,

$$p(t_p) = 1 - \left[\exp - (t_p/t_o)^m\right] , \tag{96}$$

and for $t_p < t_o$,

$$p(t_p) = (t_p/t_o)^m \quad ,$$

where m is the shape parameter and t_o is the scale parameter. The scale parameter t_o will depend on the specific mechanism of cavity growth, and will be a function of the stress level, viscosity, (diffusivity), boundary energy, etc. All cavity growth mechanisms yield times that are stress dependent and proportional to an Arrhenius factor (through a diffusivity or viscosity). Hence the scale parameter can be expressed by the general relation;

$$t_o = \zeta \sigma_\infty^{-n} \exp(Q/kT) \quad , \tag{97}$$

where Q is the activation energy for the cavity growth process, n is the stress exponent ($1 < n < 3$) and ζ is the parameter that contains the remaining cavity growth variables.

Analysis of the macrocrack formation process can now proceed by assuming that t_p is not appreciably influenced by the prior existence of cavities on adjacent facets. Then, the probability P of forming contiguous facet-sized cavities of sufficient extent to produce a macrocrack of length a (Fig. 30) can be obtained from McClintock's result [33],

$$P = \left(\frac{A_T \sqrt{p}\ \ell np}{\ell^2 (0.5 \ell np - 1)} \right) \exp[a/\ell) \ell np] \quad , \tag{98}$$

where p is the probability that a given facet has cavitated at time t and A_T is the total grain boundary area subject to the stress σ_∞. For small p (the case of present interest) combining Eqs. (96) and (98) gives the probability $P(t_i)$ of macrocrack formation at time t_i as;

$$P(t_i) = \left(\frac{2A_T}{\ell^2} \right) (t_i/t_o)^{m[0.5 + \pi K_f^2 / 4\sigma_\infty^2 \ell]} \quad . \tag{99}$$

At a specific probability level, e.g., the median level (P = 0.5), the macrocrack incubation time becomes;

$$\ell n(t_i/t_o) = \frac{\ell n(\ell^2/4A_T)}{m(0.5 + \pi K_f^2/4\sigma_\infty^2 \ell)} \quad . \tag{100}$$

For most conditions of interest in ceramics $K_c^2 \gg \sigma^2 \ell$, whereupon Eq. (100) reduces to;

$$\ell n t_i = \ell n t_o - \left(\frac{4\sigma_\infty^2 \ell}{\pi m K_f^2} \right) \ell n(4A_T/\ell^2) \quad . \tag{101}$$

Invoking the general requirement that t_o be proportional tc an Arrhenius and a stress term (Eq. (97)), Eq. (101) can be written as;

$$\ell n[t_i \exp(-Q/kT)] = \ell n\zeta - n\ell n\sigma_\infty - \sigma_\infty^2(4\ell/\pi m K_f^2)\ell n(4A_T/\ell^2) \quad , \tag{102a}$$

or

$$\ell n\theta_r = B - n\ell n\sigma_\infty - C\sigma_\infty^2 \quad , \tag{102b}$$

where θ_r is the Orr-Sherby-Dorn rupture parameter, C is a parameter that depends on the grain size and toughness and on the sample size (through A_T/ℓ^2), and B and n are constants that depend on the details of the cavity propagation process.

The appearance of Orr-Shelby-Dorn behavior is satisfying because it implies that all of the temperature effects, correlated by other investigators through this parameter, will also apply to the present model. The general shape of the failure time, stress curve predicted by Eq. (102b) is plotted in Fig. 31a. The general utility of the predicted failure time relation can be explored by plotting the logarithm of the rupture parameter θ_r as a function of σ_∞^2, and treating A, n and C as adjustable parameters (with n being confined to the range, $1 \leq n \leq 3$). The results of Walles [34] on Al_2O_3 and SiC fibers (the only comprehensive data presently available) taken from the correlation developed by Charles [35] are plotted in Fig. 31b,c. The correlation is very good. Such a correlation does not, of course, substantiate the validity of the model, because alternate models can provide correlations of nearly equal quality. It does, however, permit the model to be regarded as a serious candidate. Further experimental comparisons are presented in a subsequent section.

2.4.2 Zone spreading

The incidence of zone spreading is contingent upon the presence of appreciable constraint and the resultant development of enhanced tensions around the periphery of the initial cavitation zone. If cavitation firstly occurs along several contiguous boundaries, for which one of the parameters that dominate the cavitation rate (ψ, D_s) deviates from the average value, the local stress outside the cavitation zone, on the contiguous boundaries, then exceeds the applied stress (Fig. 30). The cavitation rates in this peripheral zone are presumably non-uniform and hence a complete solution of peripheral cavity growth constitutes a formidable problem. Nevertheless, the essence of the process can be established by adopting a simplified, intermittent spreading procedure. Cavity growth in each peripheral zone is assumed to occur

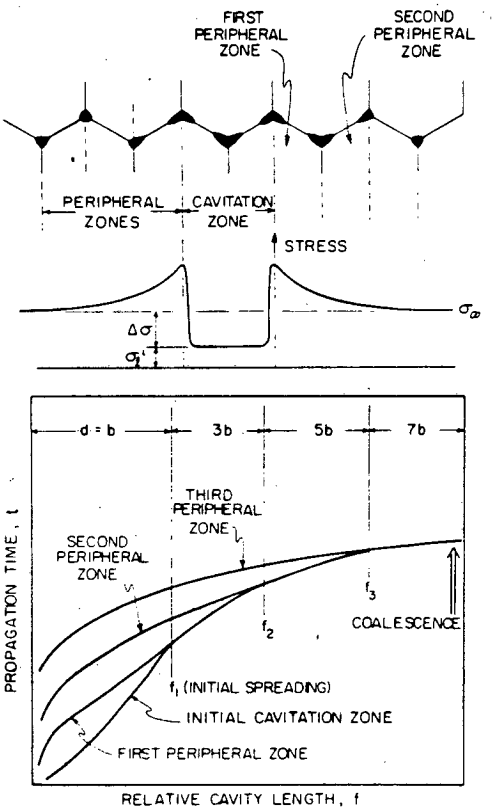

XBL816-6005

Fig. 30. A schematic of the zone spreading process.

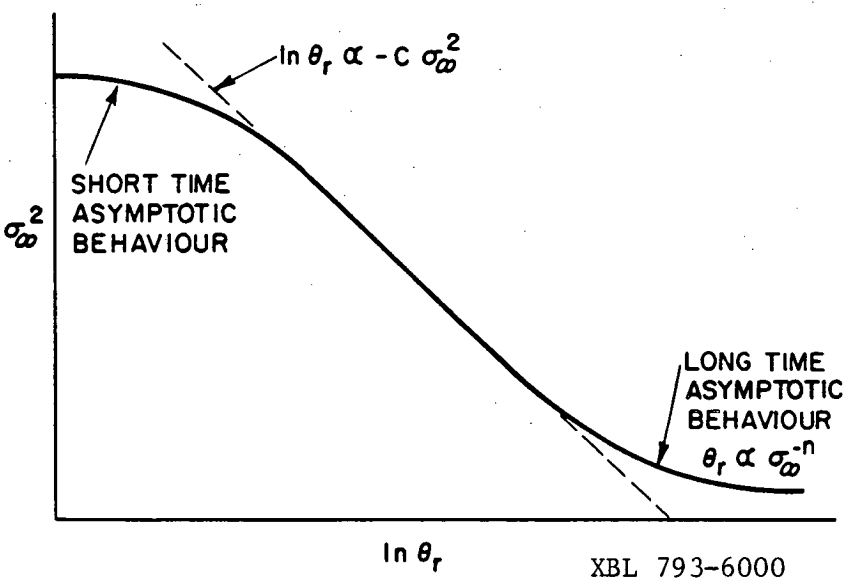

XBL 793-6000

Fig. 31a. Failure times predicted by the statistical accumulation model: schematic.

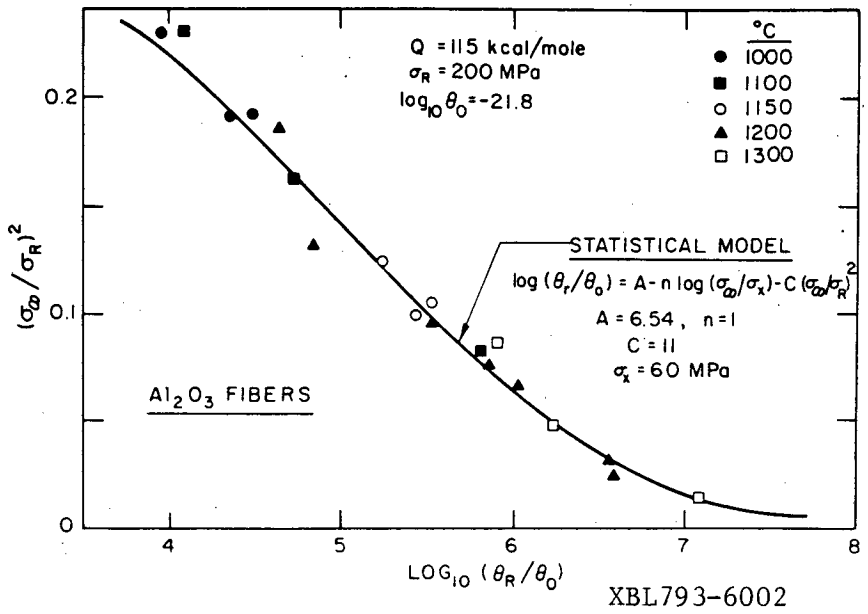

Fig. 31b. Failure times predicted by the statistical accumulation model: comparison with results for Al_2O_3 fibers.

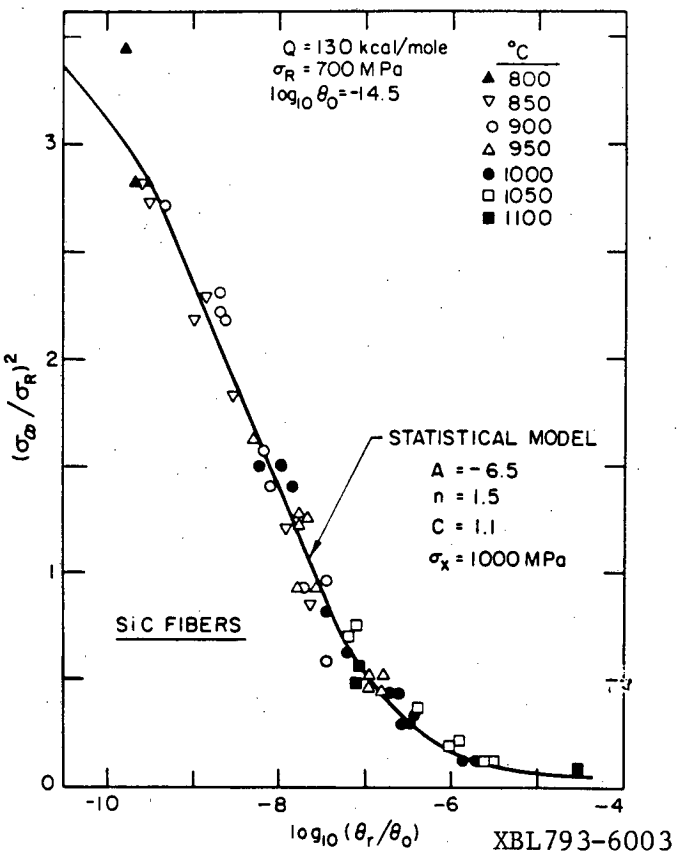

Fig. 31c. Failure times predicted by the statistical accumulation model: comparison with results for SiC fibers.

uniformly (i.e., two uniformly approaching cavities on each peripheral boundary, Fig. 30) at a stress equal to the average stress over that boundary (Eq. (11b)), while cavitation on the original boundary continues at the initially deduced local stress. Then, at a time when the cavity lengths in the cavitation zone and in the peripheral zone become equal, the cavitation zone is considered to advance to the boundary of the first peripheral zone. The process is continued by considering the growth in the next peripheral zone, with a new value of the local stress assigned to the cavitation zone (based on the increase in the zone size, d). Proceeding in this way the time t_i needed to form a discrete macrocrack can be deduced [5].

The zone spreading problem is illustrated for the case of a single phase polycrystal, for which preferred cavitation is based on local deviations in ψ or D_s (Fig. 32). The zone spreading process can be conveniently separated into three regimes. Firstly, large local deviations in the dihedral angle and in the diffusivity appear to be relatively innocuous, because cavity extension along the grain facet can proceed without the generation of appreciable stress in the peripheral zone. Hence, the cavity extends fully along the grain facet before inducing significant cavitation on the contiguous boundary (Fig. 32a). This cavitation behavior is likely to pertain in isolated regions during the early stages of failure, and explains the observation of premature full-facet sized cavities [4].

Secondly, when cavity propagation occurs in regions containing several contiguous boundaries with significant (but not large) deviations in dihedral angle, the trends in constraint (Fig. 32b) suggest continuous zone spreading. The failure time is then dictated by the spreading process and occurs relatively rapidly. Such regions consequently exert the primary influence on high temperature failure. In this circumstance, a large proportion of the failure time is consumed while cavitation is confined to a small number of contiguous grain facets. A strong interdependence of the failure time on the steady state creep rate (Monkman-Grant behavior) is thereby, anticipated, and the distribution in failure times is related primarily to the creep rate variability of the surrounding material.

Finally, it is noted that in regions of relative uniformity, cavitation develops homogeneously, by virtue of a rapid zone spreading process (Fig. 32c). The stress thus remains at a level essentially similar to the applied stress, and the unconstrained failure time relations pertain. However, failure does not evolve quickly. This behavior is not well understood; but presumably, the long failure times obtain either because cavity nucleation is inhibited in these

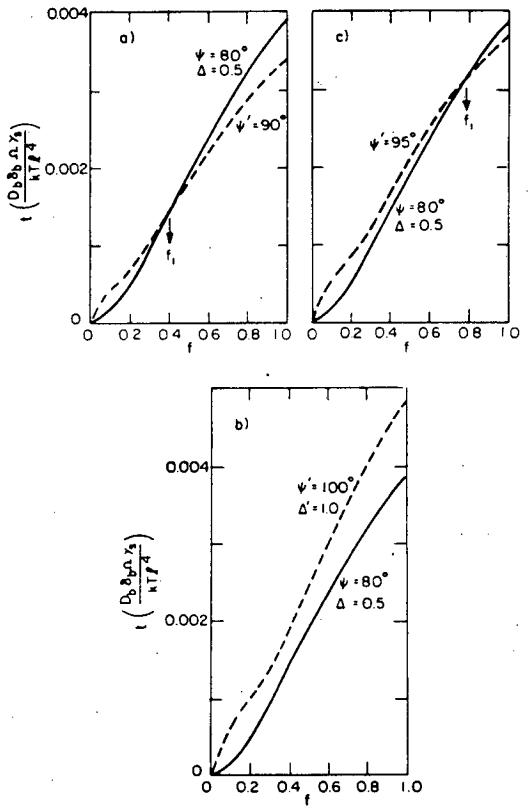

XBL814-5532

Fig. 32. Cavity propagation times in the cavitation zone and the first peripheral zone predicted for cavities growing from three grain corners.

regions (by the larger ψ) or because the larger cavitation times associated with the larger ψ or D_s are not counteracted by the loss of constraint (Fig. 32c).

3. CRACK PROPAGATION

3.1 Morphological observations

Observations of the crack tip region at relatively high applied loadings in materials subject to crack growth under creep conditions indicate the concurrent existence of a damage zone and of crack tip blunting [3,36] (Fig. 33). The damage zone, which consists of individual and coalesced cavities, is undoubtedly a consequence of enhanced cavitation rates in the crack tip stress field. The crack advance under this circumstance appears to be incremental [3]. Specifically, the crack tip remains stationary and blunts until the damage level attains a sufficient intensity that the adjacent cavities merge with the crack. This constitutes a crack advance. The process then repeats, and a quasi-steady-state velocity results. The most intense damage is generally not coplanar with the crack (Fig. 33) and consequently, the crack path is typically quite irregular (relative to the more planar crack surfaces created during brittle fracture).

At lower applied loadings the damage rate ahead of the crack decreases relative to the crack tip blunting rate. A condition is then reached wherein the crack continues to blunt without perceptible crack advance (Fig. 33), resulting in an apparent creep crack growth threshold [3,37]. The existence of the threshold is an important concept in creep crack growth. Finally, at very low load levels, crack healing may occur [36,38] (Fig. 33), by a diffusion mechanism, involving neck growth within segments of the crack surface in mutual contact.

The crack opening and blunting processes are accompanied by surface displacements that form a impression ahead of the crack (Fig. 34) and a ridge over the crack surface (Fig. 34) [3]. These displacements are related to the stress fields around the crack and thus, provide a means of characterizing the crack tip field under creep conditions.

3.2 Crack tip fields

The characterization of crack extension-rates is typically determined by the parameter that dictates the amplitude of the singular field near the crack tip. For example, stress corrosion cracking rates in elastic materials are adequately characterized by the stress intensity factor, K [39]. The situation is more complex under creep conditions [40]. The important singularity depends upon the manner in which the crack growth proceeds. For present purposes, it is

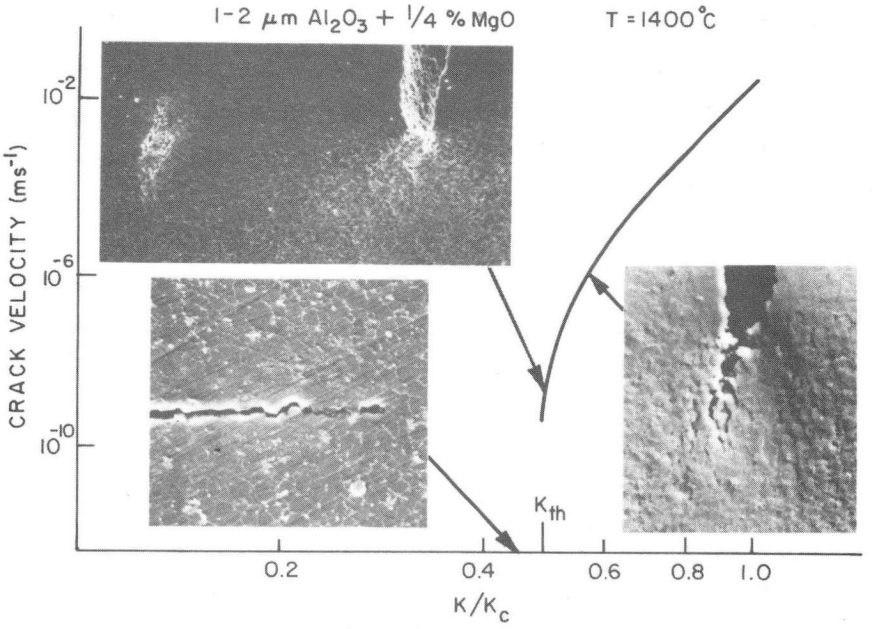

Fig. 33. A schematic illustrating the characteristic behavior of pre-existing cracks under creep conditions
(XBB810-11495)

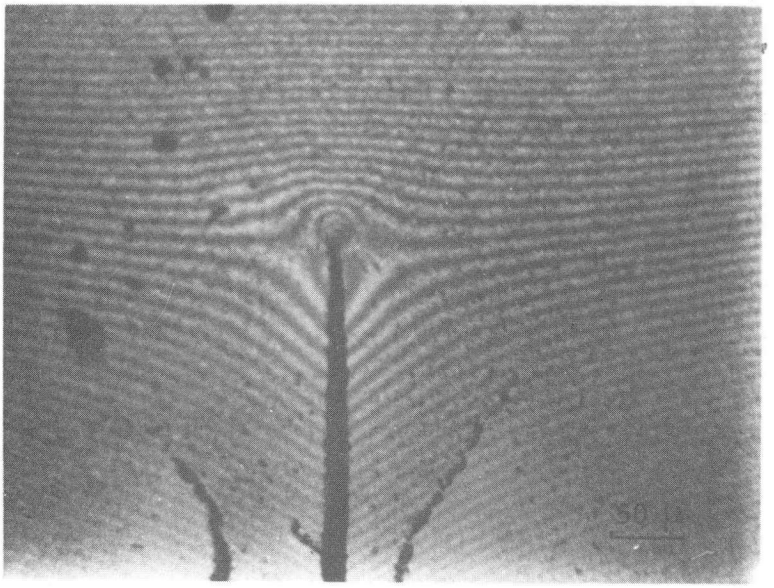

Fig. 34. Interference fringe displacements of the surface of a crept, pre-cracked Al_2O_3 illustrating the surface displacements that accompany crack blunting.
(XBB823-1956)

required that the crack advance incrementely. Hence, immediately following a crack advance, the crack tip zone is subject to primary creep, characterized by

$$\dot{\varepsilon} = \dot{\varepsilon}_{op}(\sigma/\sigma_o)^{n_p}(\varepsilon/\varepsilon_{op})^{-m} \quad , \tag{103}$$

where n_p and m are primary creep exponents and ε_{op}, σ_o and ε_{op} are primary creep coefficients. The crack tip field under primary creep conditions is given by;

$$\sigma_{ij}/\sigma_o \propto [C_p(t)/r]^{(m+1)/(m+n_p+1)} \quad , \tag{104}$$

where r is the distance from the crack tip and $C_p(t)$ is the stress field amplitude. If the primary creep field is embedded in an elastic field (a likely situation following a crack increment), then;

$$C_p(t) = \frac{K^2(1-\nu^2)}{E}\left[\frac{m+1}{(m+n_p+1)t}\right]^{1/(m+1)} \quad , \tag{105}$$

where E is Young's modulus and ν is Poisson's ratio. The amplitude is thus expressible in terms of a time modified K[vi]. Hence, if crack advance occurs while primary creep prevails at the crack tip, and before the creep front advances to the specimen boundaries, the crack velocity should be adequately characterized by K.

For larger intervals following crack advance, the primary creep region will extend to the specimen boundaries and secondary creep will prevail at the crack tip,

$$\dot{\varepsilon} = \dot{\varepsilon}_{os}(\sigma/\sigma_o)^{n_s} \quad , \tag{106}$$

where n_s and ε_{os} are the secondary creep parameters. The crack tip field is then characterized by

$$\sigma_{ij}/\sigma_o \propto [C_s(t)/r]^{1/(1+n_s)} \quad , \tag{107}$$

where

$$C_s(t) = \left[\frac{(n_s+m+1)C_p(t)}{(m+s)(n_s+1)}\right] t^{-m/(m+1)} \quad .$$

(vi) J would be more appropriate if the far field were subject to plastic deformation.

However, the far field is dictated by a primary creep region rather than an elastic region and K is thus an inadequate loading parameter. The crack growth behavior is best approximated by the asymptotic value of C_p;

$$C_p^* = \lambda a \sigma_\infty^{(m+n_p+1)/(m+1)} , \qquad (108)$$

where σ_∞ is the applied stress, a is the crack length and λ is a proportionality constant that depends on the primary creep parameters and the far field loading.

Ultimately, for long crack advance waiting periods, as pertinent to low crack velocities, steady-state creep prevails throughout the specimen. The crack tip field is still characterized by Eq. (107), but now C_s can be related to the applied loading by the time independent parameter;

$$C_s^* = F_s \sigma_s \dot{\varepsilon}_{os} a (\sigma_\infty/\sigma_o)^{1+n_s} , \qquad (109)$$

where F_s is a parameter that depends on the specimen geometry and loading.[vii] Note that, for $n_s = 1$,

$$C_s^* \propto a\sigma_\infty^2 \equiv K^2/\pi , \qquad (110)$$

and the stress amplitude at the crack tip is uniquely determined by K. For typical practical ceramics, $1 < n_s < 2$ [1,24]; hence K should be a reasonable correlating parameter for most crack growth data. However, some non-uniqueness should be expected at low crack velocities, where C_s^* provides a more appropriate association between the crack tip field and the applied loading.

3.3 Crack growth data

Most high temperature crack growth data for ceramics have been evaluated using K as the appropriate loading parameter. The uniqueness of K has been confirmed at high crack velocities [41], but its utility at low velocities has yet to be fully explored. However, crack opening and surface displacement measurements performed on polycrystalline Al_2O_3 [36] suggest the approximate validity of K (and of the linear stress field amplitude) at relatively low applied loadings; as demonstrated by good correlations with the crack tip displacement field expected for a linear material (Fig. 35); despite the non-linearity of the creep rate ($n \approx 1.8$) measured at low strain rates.

[vii] The equivalent parameter for elastic loading is, $F_E = K/\sigma\sqrt{\pi a}$.

Several interesting features emerge from the existent crack growth data. The critical stress intensity factor for single phase materials, K_{IC}, decreases with increase in temperature, but can increase in materials that contain a continuous amorphous second phase at the grain boundaries [42]. The crack growth susceptibility increases as the temperature increases or as the viscosity of amorphous second phases decreases [43]. Consequently, the exponent n_v that characterizes the crack velocity, v,

$$v/v_o = (K/K_{IC})^{n_v} , \qquad (111)$$

can exhibit a wide range of values (typically $6 < n_v < 10^3$), dependent upon temperature and composition [37]. Adequate crack growth models must account for this range of possibilities. Finally, an apparent crack growth threshold is observed [37], and probably relates, as noted above, to dominance of the crack tip blunting rate (relative to the damage rate ahead of the crack).

3.4 Crack growth models

Explicit crack growth models exist for cracks extending along the boundary between two grains by a process involving surface and grain boundary diffusion [44] (Fig. 36). The analysis predicts that [44]

$$K/K_G = 0.85 \left[(v/v_{min})^{1/12} + (v/v_{min})^{-1/12}\right] , \qquad (112)$$

where

$$K_G^2 = E(2\gamma_s - \gamma_b)(1-\nu^2) ,$$

$$v_{min} = 8(D_s\delta_s)^4 \Omega[E/(1-\nu^2)D_b\delta_b]^3/kT\gamma_s^2 .$$

This relation anticipates a threshold K (Fig. 36), as well as conforming with selected data. However, the mechanism is not representative of the crack growth behavior in polycrystalline aggregates; a process which involves incremental crack advance into a damage zone. An alternate, damage-zone, model is thus required.

A comprehensive damage zone model should incorporate the following features. The crack tip field in the absence of damage should be expressible in terms of K, C_p^* or C_s^*, depending upon the waiting period for crack advance. The damage should reduce the stress in vicinity of the crack tip by virtue of constraint on the local volume expansion by the surrounding material. The stress at the crack tip should be consistent with chemical potential continuity where grain

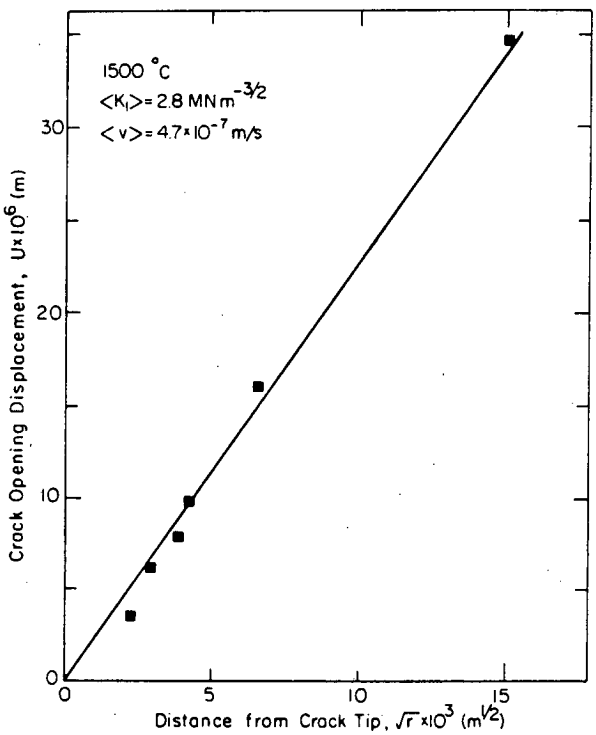

Fig. 35. Creep crack opening displacement measured on an Al_2O_3 specimen. (XBL822-5251)

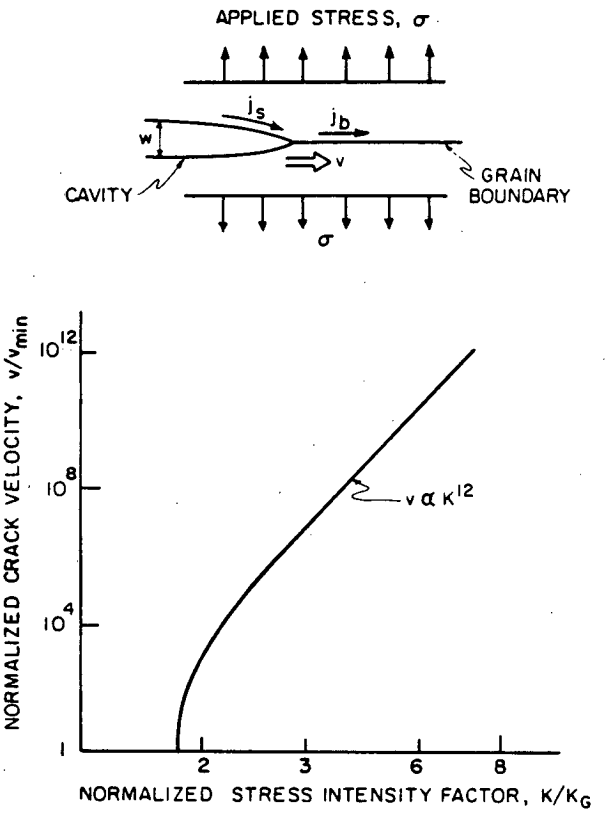

Fig. 36. Crack velocity behavior predicted for a single crack in a bicrystal. (XBL816-6009)

boundaries emerge at the crack surface. The damage should be in the form of grain boundary cavities activated by the normal stress; a requirement which would induce non-coplanar cavitation,[viii] in accord with observation. Opening of the crack and coalescence with the cavities (to constitute a crack advance) should incorporate grain boundary sliding. Such a comprehensive model has not been developed. However, certain of the important requirements have been invoked in several recent attempts. Bassani [40] has examined the growth of an individual coplanar cavity within the various important singular fields. However, constraint effects have not yet been incorporated. Raj and Baik [45] have developed a bi-crystal model with coplanar damage (Fig. 37). The stress field amplitude is considered to be dictated by K and the growth of the damage is allowed to relax the stress near the crack tip. The crack is assumed to advance when the cavities coalesce with the crack tip. A threshold is also invoked, based on the threshold stress for cavity nucleation.

Finally, Tsai and Raj [28] have developed a generalized damage zone concept. The elements of this model undoubtedly provide the closest available representation of creep crack growth by a damage mechanism. The model invokes a damage zone size, z_d, that exists in quasi-steady state when the crack is propagating at a velocity v. The crack growth rate can consequently be expressed in terms of the time, t_g, taken to form full-facet cavities of the zone periphery, because steady state requires that the crack tip advance by one facet length, ℓ, when the time t_g has expired ($v = \ell/t_g$). The time t_g may be computed by determining the stress at the damage zone boundary and inserting this stress into the specific relation that characterizes the active cavity growth mechanism (section 2.3). This procedure requires recognition of the effect on the stress at z_d of both the principal crack and the intervening damage. For a linear material, the stress is given by;

$$\sigma_\ell \approx [K/\sqrt{2\pi z_d}]\ g\ (e_{ij}^T) \quad , \tag{113}$$

where g is a function of the cavitation strain e_{ij}^T within the damage zone.

[viii] The maximum tension ahead of a crack occurs at an orientation $\theta \approx \pi/3$.

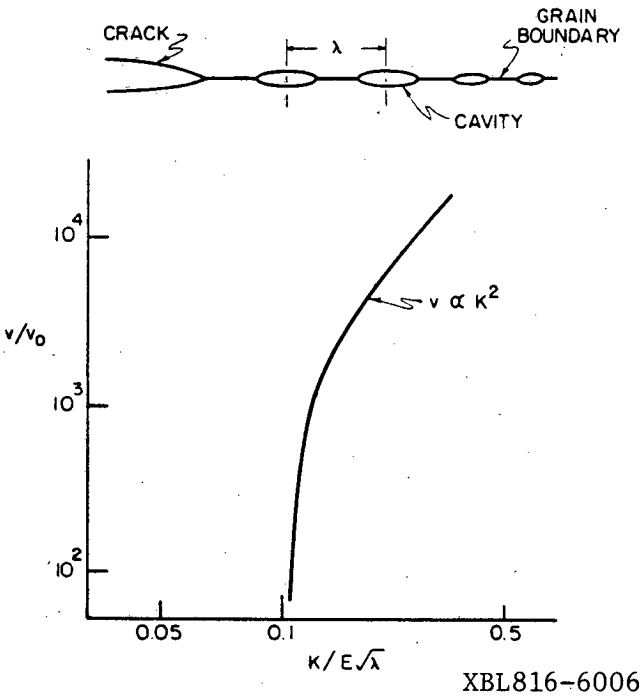

Fig. 37. Crack velocity behavior predicted for a cavity coalescence process of crack advance within a bicrystal.

Precise determination of σ_ℓ are mechanism dependent. For example, mechanisms involving the growth of very narrow crack like-cavities (section 2.3) allow the intervening material to be analyzed as an elastic body containing an array of microcracks. The stress field may then be computed using one of several established techniques that allow for the interaction between the principal crack and the microcrack damage [46,47].

Damage zone size determination is also mechanism dependent. The most plausible determinant of the zone size is the level of the local stress (or strain) vis-a-vis the critical cavity nucleation stress (section 2.2). An approximate solution for z_d, based on the assumption of a Dugdale zone [48] within a linear material, subject to a initial stress σ_c, yields a stress independent zone size,

$$z_d \approx (\pi/8)\,(K^*_{th}/\sigma_c)^2 \quad , \tag{114}$$

where K_{th}^* represents the threshold stress intensity at which damage begins to form ahead of the crack tip. Both K_{th}^* and σ_c are mechanism dependent. More precise formulations based on a variable stress within the damage zone would result in a stress dependent damage zone size.

Combining the zone size relation (Eq. 114) with the local stress (Eq. 113) gives;

$$(\sigma_\ell/\sigma_c) \approx (2/\pi)\,(K/K^*_{th})g(e^T_{ij}) \quad . \tag{115}$$

Inserting Eq. (115) into the appropriate cavity growth relation (section 2.3) yields t_g and hence, v. The presence of an extended damage zone minimizes the constraint at the zone boundary. Hence, expressions for unconstrained cavity propagation can be applied. For example, if cavitation is dominated by the equilibrium growth of the cavity from a three grain corner, Eq. (47), the crack propagation rate becomes;

$$v = \frac{160\sqrt{3}}{\pi}\left(\frac{\Omega D_b \delta_b \sigma_c g(e^T_{ij})}{kT\ell^2 F(\psi) K^*_{th}}\right) K \quad . \tag{116}$$

This result illustrates that the assumption of a Dugdale zone yields a stress intensity factor exponent, n_v, similar[ix] to the stress exponent for the underlying cavity growth mechanism. It is thus unlikely to account for the large range in n_v that obtains for crack propagation in ceramic polycrystals. A more comprehensive treatment of the stress within the damage zone would thus appear to be a prerequisite for the adequate modelling of creep crack growth in ceramics. (Unless the range of n_v is associated with asymptotic approach to the threshold).

3.5 Crack propagation times

Experimentally determined relations between the crack growth rate and the stress intensity factor (Eq. (111)) can be used to predict that component of the failure time attributed to macrocrack propagation [42]. This is achieved by noting that the stress intensity is related to the applied loading by;

$$K = \sigma_\infty Y\sqrt{a} \quad , \tag{117}$$

where Y is a geometric parameter ($2/\sqrt{\pi}$ for a penny-shaped flaw). Differentiating to obtain;

$$dt = \frac{2}{\sigma_\infty^2 Y^2}\left(\frac{K}{v}\right) dK \quad , \tag{118}$$

and integrating between K_f (the stress intensity that characterizes the occurence of a discrete macrocrack) and the critical stress intensity factor, K_c, then gives the crack propagation time;

$$t_c = \frac{2}{Y^2}\int_{K_f}^{K_c}\left(\frac{K}{\sigma v}\right) dK \quad . \tag{119}$$

Inserting the crack growth rate relation given by Eq. (111), the crack propagation time at constant stress becomes,

$$t_c = \frac{2K_c^{n_v}}{\sigma_\infty^2 Y^2 v_o (n-2)}\left[\frac{1}{K_f^{n_v-2}} - \frac{1}{K_c^{n_v-2}}\right], \tag{120}$$

which, for large n_v and $K_c >> K$ becomes;

$$t_c \approx \frac{2}{v_o(n_v-2)}\left(\frac{K_c}{\sigma_\infty Y}\right)^2\left(\frac{K_c}{K_f}\right)^{n_v-2} \quad . \tag{121}$$

[ix] ${e_{ij}}^T$ exhibits some dependence on K and may thus cause the K exponent in Eq. (116) to deviate from unity.

An accurate definition of K_f is thus of crucial importance to the prediction of crack propagation times. Specifically, if the nucleation process yields a discrete crack when K_f is a specified fraction of K_c (as proposed in section 2.4.1), the the stress dependence of the propagation time must be uniquely characterized by the simple proportionality;

$$t_c \propto \sigma_\infty^{-2} \quad . \tag{122}$$

Alternatively, in the presence of pre-existent cracks with an initial stress intensity, $K_i > K_{th}$, the crack propagation time becomes;

$$t_c \approx \frac{2a_i^{-(n_v-2)}}{v_o(n_v-2)} \left(\frac{K_c}{\sigma_\infty Y}\right)^{n_v} \quad . \tag{123}$$

A much larger stress exponent, $t_c \propto \sigma_\infty^{-n}$ thus obtains and the failure time depends upon the initial magnitude, a_i, of pre-existing cracks (as characterized by proof testing or NDE).

4. PREMATURE FAILURE FROM LARGE SCALE INHOMOGENEITIES

There are several important microstructural sources of premature high temperature failure in ceramics; especially zones of exceptional grain size and isolated amorphous regions in otherwise single phase material. A large grained region in a fine-grained solid subject to creep deformation has a higher viscosity than the matrix, because of the strong grain size dependence of the creep rate (either Herring-Nabarro or Coble creep). This region, and the surrounding fine-grained matrix, must therefore experience stresses in excess of the applied stress, by up to $\sim 2\sigma_\infty$ [22] (Fig. 38). This enhanced tension can accelerate the cavity propagation process and thus prematurely initiate a crack. The magnitude of the effect can be discerned by incorporating the stress concentration factor into the cavity propagation times derived in section 2. Generally, the maximum reduction in crack nucleation times is in the range, 2-4, depending upon the stress dependence of the dominant cavitation mechanism [22]. Fine grained, or amorphous, zones can also induce stress concentrations of similar magnitude within the surrounding material and reduce the crack nucleation time to a comparable extent (2-4). Additionally, however, the potential for a reduced cavity spacing in fine-grained or amorphous zones (vis-a-vis the surrounding matrix) can cause rapid internal failure of these zones, despite the reduced local stress level. For example, cavitation occurring from three grain edges within a fine grained zone can cause

internal failure of the zone at times up to an order of magnitude less than the time needed to induce a crack in the coarse grained matrix. The maximum reduction in local rupture time occurs when the grain size ratio is ~0.2 and the stress within the fine grained region is 0.1 σ_∞. However it is emphasized that internal rupture of this region does not necessarily result in premature failure because the rupture must be capable of extending into the matrix. This topic has not yet been addressed. But, presumably, the stress intensity associated with the local rupture should exceed K_{th} in order to induce eventual failure.

Large amorphous regions may exert an additional detrimental influence on the high temperature failure resistance of ceramics: especially when the amorphous phase exhibits good wetting characteristics and is capable of rapid viscous flow. Then, the amorphous material can flow into cavities created within the solid phase and accelerate their growth. This may be achieved by reducing the dihedral angle (based on good wetting characteristics) and enhancing the matter transport rate from the cavity surface to the cavity tip (i.e., an effective increase in $D_s\delta_s$). For example, noting that the crack-like cavity propagation times at high stress levels (Eqs. (46) and (50a)) are characterized by, $t_p \propto \sin^{3/2}(\psi/4)(D_s\delta_s/D_b\delta_b)^{1/2}$, a perfectly wetting amorphous phase ($\psi \sim 0$) is predicted to reduce the propagation time to ~0 by allowing the formation of crack-like cavities of negligible width. The propagation times are then limited by the flow rate of the viscous material into the cavity, in accord with the principles discussed in section 2.3.2. This process would allow the amorphous zone to spread along a plane normal to the applied tension and thereby induce a substantial reduction in the failure time. The details of this process have not yet been evaluated.

5. INTERPRETATION OF EXPERIMENTAL RESULTS

Plots of the available creep rupture data for ceramics, using logarithmic scales, (Fig. 39) indicates that the temperature dependence of the failure time can be adequately incorporated into an Arrhenius parameter, as anticipated by both the Monkman-Grant and Orr-Sherby-Dorn parameter. The stress exponents, n, are mostly in the range 3-6, except for sintered SiC [49] which has an exponent of ~30. The latter is undoubtedly a consequence of crack propagation controlled failure [50]; while the smaller n values are probably associated with crack nucleation controlled failure. However, explicit correlations with the failure models pertinent to nucleation controlled rupture are limited by the paucity of ancilliary data, such as creep rates and diffusivities. Before embarking upon a closer scrutiny of specific rupture results, it is appropriate to recognize the data correlation

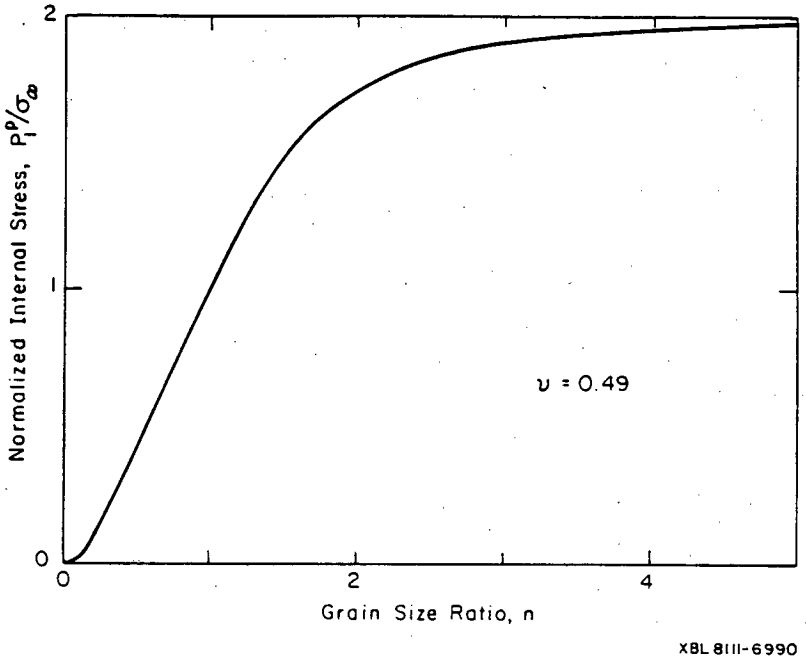

Fig. 38. The stress concentration that develops within a large grained region.

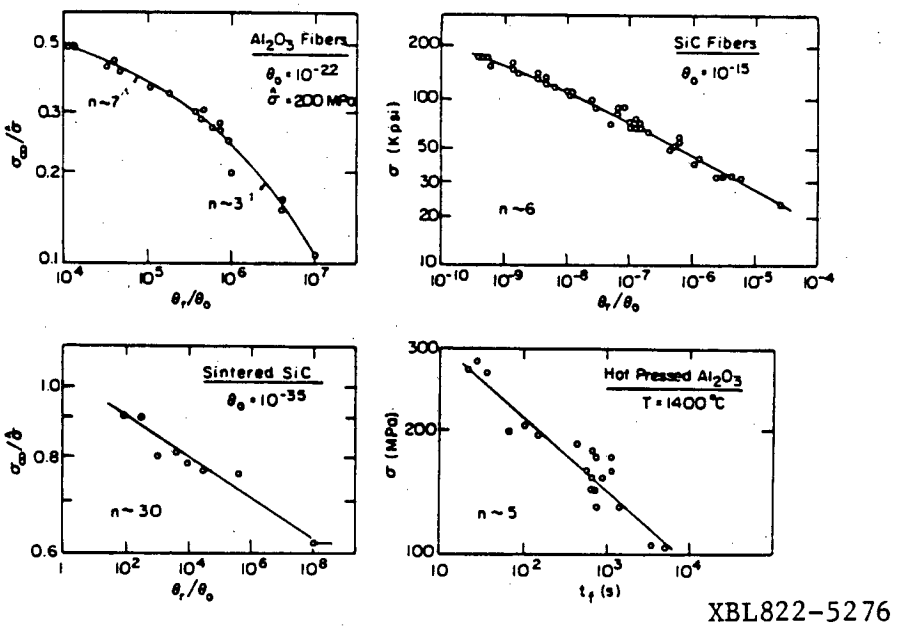

Fig. 39. A summary of creep rupture data for polycrystalline ceramics.

scheme devised by Charles [35]. Based upon an assumption of crack propagation controlled failure and a hypothesized crack growth rate relation,

$$\dot{a} = (D/a)\exp[\beta(2\sigma_\infty\sqrt{a/\rho} - \gamma_s/\rho)] \quad , \qquad (124)$$

where D is a diffusivity, β is a coefficient and ρ is the crack tip radius, the rupture time t_r was derived as;

$$t_r e^{-Q/kT} = \theta_o(N^3/R+3N^2/R^2+6N^3+6/R^4)\,(N^3+3N^2+6N+6)^{-1} \quad , \qquad (125)$$

where θ_o and N are fitting parameters unique to a specific material and R is the ratio, $\hat{\sigma}/\sigma_\infty$, where $\hat{\sigma}$ is the intrinsic (zero time) strength of the material. All available creep rupture data for ceramics can be fitted by Eq. (125), which thus presents a useful basis for comparing the creep rupture performance of different materials. However, more specific inferences, concerning data extrapolation and underlying mechanisms, should be treated with caution.

A mechanistic interpretation of the rupture data ultimately requires subsidiary microstructural information. Interpretation attempted in the absence of such information should be regarded as speculative. It is tempting to account for the observed stress rupture exponent by invoking the unconstrained, low stress, crack-like cavity growth process (n = 3). However, the experimental results have been obtained in a stress range ($\sigma_s\ell/\gamma_s \sin(\psi/4) > 10$) that appreciably exceeds the stresses at which this mechanism ostensibly operates. An interpretation based on crack-like cavity growth should thus be regarded cautiously, in the absence of discrete information concerning cavity shapes. An alternative interpretation, based on the Monkman-Grant relation, is also without basis, because creep rate information has not generally been obtained on the same materials used to determine rupture characteristics. In the one instance (fine grained Al_2O_3) where comparative creep rate and creep rupture data has been acquired the creep exponent ($n_s = 1.8$) is not large enough to account for the stress dependence of the rupture time ($n \approx 5$) and a simple Monkman-Grant relation (e.g., based on highly constrained equilibrium cavity growth) does not appear to rationalize the data.

The compatibility of the available failure data with the probabilistic model of unconstrained cavity growth and coalescence (Fig. 31), is not a sufficient basis for acceptance of a probabilistic interpretation; the parameters of the model must also be consistent with the basic mechanisms of cavity growth. Also, the predicted existence of specimen size

effects requires substantiation. The necessary mechanistic information is exemplified by attempting to interpret the rupture data obtained for the Al_2O_3 fibers. Assuming that the Al_2O_3 contains a continuous thin amorphous phase (typical of liquid phase sintered Al_2O_3) and that failure occurs by hole growth within the second phase, the probabilistic model predicts [31]

$$\ell n\theta_r = \ell n[0.3\eta_o(\ell/\delta_o)^2] - \ell n\sigma_\infty - \sigma_\infty^2(4\ell/\pi m K_f^2)\ell n(4A_T/\ell^2) \quad , \tag{126}$$

where η is the viscosity coefficient ($\eta=\eta_o e^{-Q_\eta/kT}$). Correlation of Eq. (126) with the test data for Al_2O_3 fibers (Fig. 31b) is achieved by firstly evaluating the mechanistic parameters from the test data;

$$(4\ell/\pi\eta K_f^2)\ \ell n(4A_T/\ell^2) = 3 \times 10^{-16}\ N^2 m^{-1} \quad , \tag{127a}$$

$$\log\ [0.3\eta_o(\ell/\delta_o)^2] = -5.5 \quad . \tag{127b}$$

Then, by inserting the pertinent dimensional information (area tested, $\sim 1.2 \times 10^{-5}$ m^2, grain facet length, 5μm) the consistency of the remaining microstructral parameters can be assessed. For example, assuming that $m \approx 1$ (as determined from creep tests on liquid phase sintered Si_3N_4) [31], Eq. (127a) gives $K_f \approx 0.5$ MPa$\sqrt{m}$; which compares with $K_c \approx 2$ MPa$\sqrt{m}$ for typical polycrystalline aluminas at comparable test temperatures. Additionally, by assuming that $\delta_o \approx 5$ nm (as, again, observed for Si_3N_4) Eq. (127b) yields a viscosity coefficient $\eta_o \approx 10^{-1}$ poise, which in conjunction with the experimentally determined activation energy (Q_η = 115 kcal/mole), gives a resultant viscosity [31] within an order of magnitude of the viscosity of SiO_2 (a predominant second phase constituent in liquid phase sintered Al_2O_3). This correlation is, of course, based on too many assumed parameters (although, all of the parameters exhibit reasonable values); but it illustrates the detailed microstructural information needed to substantiate failure models and consequently, to develop a prediction capability.

6. IMPLICATIONS AND CONCLUSIONS

The observations and analysis of high temperature cavitation summarized in the present review indicate the inhomogeneous nature of high temperature failure in ceramics. A possible consequence of the inhomogeneity (and the resultant development of constraint) is the inverse dependence of the failure time on the steady-state creep rate of the material (Monkman-Grant behavior). Under crack nucleation controlled

conditions within this regime, any microstructural modification that reduces the creep rate should thus produce a proportional increase in the failure time. This correlation provides an invaluable basis for the design of failure resistant microstructures.

Monkman-Grant behavior may be violated under certain conditions; notably especially in the presence of a high proportion of cavitation susceptible boundaries. Constraint effects are then minimal and crack nucleation controlled failure is based on the statistical accumulation of contiguous cavities. A probabilistic analysis of this process indicates that failure in this instance is governed by an Orr-Sherby-Dorn parameter, such that the activation energy term in the parameter is related to that for the dominant cavitation process.

The failure times in both the Monkman-Grant and Orr-Sherby-Grant regimes are predicted to depend on several microstructural characteristics. In single phase materials, low values of the dihedral angle and of surface diffusivity are found to be deleterious. Low dihedral angles (high grain boundary energies) may be inevitable in ceramics (by virtue of covalent or ionic bonding characteristics). However, there may be important influences (both beneficial and deleterious) of solutes, which merit further study. A low surface diffusivity may also be inevitable for typical ceramics, as required for the initial stage sintering. But again, explorations of the temperature dependence of the diffusivity and of solute effects may indicate situations which retard cavitation without detracting from the sinterability.

In two phase materials with a continuous second phase, the predominant material variables are the thickness of the second phase, its viscosity, and the diffusivity of the major second phase constituent. Large values of the second phase thickness and diffusivity, or low viscosities, encourage rupture, as might be intuitively expected. Chemical control is thus a central concern for the creep rupture of these materials.

It also has been demonstrated that several important sources of premature crack nucleation can exist in typical ceramics:[x] in particular, zones of amorphous material in otherwise single phase materials and atypically grained zones. Premature failure results from the development of stress concentrations and/or region of high local cavitation

---

[x] It is notable that these heterogeneities differ in character from those that typically dictate the brittle fracture process at lower temperatures.

susceptibility. The elimination of large scale heterogeneities is thus an essential requirement for the prevention of premature failure.

Crack nucleation controlled creep rupture is expected to pertain to long lifetime behavior, particularly at elevated temperatures. However, the conditions that cause failure to be dominated by crack nucleation, rather than crack propagation, are still rather nebulous; although, observations of crack propagation thresholds begin to suggest crack tip blunting effects which distinguish nucleation control from propagation control.

When crack growth controls failure (as might be expected, for example, in the presence of surface cracks subject to stress intensity levels in excess of the threshold), a characterization of the crack growth rates in term of C_s^* (or K) provides a basis for predicting failure. However, effects of microstructure on the observed crack growth rates have yet to be adequately modelled.

The paucity of comprehensive creep rupture data, and of concomittant microstructural information, obtained on ceramic polycrystals has limited the present ability to distinguish the conditions of stress, temperature and microstructure that dictate the dominant operative realms of the various cavitation mechanisms. Future study should focus upon the acquisition of reliable creep rupture data and the concurrent determination of the important microstructural parameters.

REFERENCES

1. CANNON, R.M., RHODES, W.H. and HEUER, A.H. - Jnl. Amer. Ceram. Soc., 1980, 63, 46.

2. HEUER, A.H., TIGHE, N.J. and CANNON, R.M. - Jnl. Amer. Ceram. Soc., 1980, 63, 53.

3. EVANS, A.G. and BLUMENTHAL, W. - Fracture Mechanics of Ceramics (Eds. R.C. Bradt, D.P.H. Hasselman, F.F. Lange, and A.G. Evans), Plenum, N.Y., 1982, vol. 5.

4. PORTER, J.R., BLUMENTHAL, W. and EVANS, A.G. - Acta Met., 1981, 29, 1899.

5. HSEUH, C.H. and EVANS, A.G. - Acta Met., 1981, 29, 1907.

6. SOLOMAN, A.A. and HSU, F. - Jnl. Amer. Ceram. Soc., 1980, 63, 467.

7. DJEMEL, A., CADOZ, J. and PHILIBERT, J. - 'Creep and Fracture of Engineering Materials and Structures' (Eds. B. Wilshire and D.R.J. Owen), Pineridge, U.K., 1981, p. 381.

8. FOLWEILER, R.C. - Jn. Appl. Phys., 1961, 32, 773.

9. DYSON, B.F. - Can. Met. Quart., 1979, 18, 31.

10. RICE, J.R. - Acta Met. 1981, 29, 675.

11. ESHELBY, J.D. - Proc. Roy. Soc., 1957, A241, 376.

12. RAJ, R. and ASHBY, M.F. - Met. Trans., 1971, 2, 1113.

13. RAJ, R. and ASHBY, M.F. - Acta Met., 1975, 23, 653.

14. CLARKE, D.R. - Ultramicroscopy, 1979, 4, 33.

15. MARION, J., EVANS, A.G., CLARKE, D.R. - to be published.

16. FISHER, J.C. - Jnl. Appl. Phys. 1958, 19, 1062.

17. CHEN, I.W. and ARGON, A.S. - Creep and Fracture of Engineering Materials and Structures, ibid., p. 289.

18. EVANS, A.G., RICE, J.R. and HIRTH, J.P. - Jnl. Amer. Ceram. Soc., 1980, 63, 368.

19. BURTON, B. - 'Diffusional Creep of Polycrystalline Materials,' Trans. Tech. Publ., 1977.

20. CHUANG, T.J. and RICE, J.R. - Acta Met., 1973, 21, 1625.

21. CHUANG, T.J., KAGAWA, K., RICE, J.R. and SILLS, L. - Acta Met., 1979, 27, 265.

22. JOHNSON, S.M., BLUMENTHAL, W.R. and EVANS, A.G., - to be published.

23. PHARR, G.M. and NIX, W.D. - Acta Met., 1979, 27, 1605.

24. LANGE, F.F., CLARKE, D.R., DAVIS, B.I. - Jnl. Mater. Sci., 1980, 15, 601.

25. NIX, W.D. and GOODS, S.H. - 'Fracture', (ed. D. Taplin), University of Waterloo Press, 1977, vol. 2, p. 613.

26. FIELDS, R.J. and ASHBY, M.F. - Phil. Mag., 1976, 33, 33.

27. RAJ, R. and CHYUNG, C.K. - Acta Met., 1981, 29, 159.

28. TSAI, S. and RAJ, R. - to be published.

29. RAJ, R. and DANG, C.H. - Phil. Mag., 1975, 22, 909.

30. EVANS, A.G. - Acta Met., 1980, 28, 1155.

31. EVANS, A.G. and RANA, R. - Acta Met., 1980, 28, 129.

32. STROH, A.N. - Adv. Phys., 1957, 6, 418.

33. McCLINTOCK, F.A. - 'Fracture Mechanics of Ceramics', ibid., 1974, vol. 1, p. 93.

34. WALLES, K.F.A. - Proc. Brit. Ceram. Soc., 1972, 15, 157.

35. CHARLES, R.J. - 'Fracture Mechanics of Ceramics', ibid., 1978, vol. 4, p. 623.

36. BLUMENTHAL, W. - MS Thesis, University of California, Berkeley, 1981, LBL report.

37. LEWIS, M.H., KARUNARATNE, B.S.B., MEREDITH, J. and PICKERING, C. - 'Creep and Fracture of Engineering Materials and Structures', ibid., 1981, p. 365.

38. EVANS, A.G. and CHARLES, E.A. - Acta Met., 1977, 25, 919.

39. WIEDERHORN, S.M. - 'Fracture Mechanics of Ceramics', ibid., 1976, vol. 2, p. 613.

40. BASSANI, J.L. - 'Creep and Fracture of Engineering Materials and Structures', ibid., p. 329.

41. EVANS, A.G., RUSSELL, L.R. and RICHERSON, D.W. - Met. Trans., 1975, 6A, 707.

42. EVANS, A.G. and LANGDON, T.G. - Prog. Mater. Sci., 1976, 21, 171.

43. EVANS, A.G. and WIEDERHORN, S.M. - Jnl. Mater. Sci., 1974, 9, 270.

44. CHUANG, T.J. - Jnl. Amer. Ceram. Soc., 1982, 65, 93.

45. RAJ, R. and BAIK, S. - Metal. Science, 1980, 385.

46. McCLINTOCK, F.A. and MAYSON, H.J. - ASME Applied Mech. Conf., June 1976.

47. HOAGLAND, R.G. and EMBURY, J.D. - Jnl. Amer. Ceram. Soc., 1980, 63, 404.

48. DUGDALE, D.S. - Jnl. Mech. Phys. Solids, 1960, 8, 100.

49. TRANTINA, G.G. and JOHNSON, C.A. - Jnl. Amer. Ceram. Soc., 1975, 58, 344.

This report was done with support from the Department of Energy. Any conclusions or opinions expressed in this report represent solely those of the author(s) and not necessarily those of The Regents of the University of California, the Lawrence Berkeley Laboratory or the Department of Energy.

Reference to a company or product name does not imply approval or recommendation of the product by the University of California or the U.S. Department of Energy to the exclusion of others that may be suitable.

TECHNICAL INFORMATION DEPARTMENT
LAWRENCE BERKELEY LABORATORY
UNIVERSITY OF CALIFORNIA
BERKELEY, CALIFORNIA 94720